東京大学 大学院新領域創成科学研究科
基盤科学研究系
先端エネルギー工学専攻

平成 19 年度

修士論文

Structural analysis of a microwave supported detonation wave

― マイクロ波支持爆轟波の構造解析 ―

2008 年 2 月提出
指導教員 小紫 公也 准教授

66212 柴田 鉄平

Acknowledgement

I would like to gratitude to Associate Professor Kimiya Komurasaki. He gave me a theme with challenge worth and a substantial academic research environment. I could try studies with his severe but appropriate advice. And I received the many opportunity of presentation about my research. I would like to appreciate the support from Professor Yoshihiro Arakawa (Department of Aeronautics and Astronautics).
Dr. Keishi Sakamoto (Plasma Heating Laboratory, Naka fusion research center, Japan Atomic Energy Agency) gave us precious opportunities of experiments at JAEA. On the operation of gyrotron Dr. Ken Kajiwara, Dr. Ryutaro Minami, Mr. Shinji Komori, and Mr. Yukiharu Ikeda helped us. I'm so grateful to JAEA members.
I learned way of research, way of writing etc. from Mr. Oda. Whatever I say, it is not enough, but I would like to thank him.
It was my pleasure to strive to research with all members of Arakawa-Komurasaki laboratory.

Contents

List of figures

Chapter 1

Introduction

1.1 Beamed energy propulsion

Space development needs huge cost. Especially launch cost is enormous. Its cost prevents space utilization from spreading. Cause of the huge cost is a chemical rocket which uses energy of combustion and is now mainstream launch method. Its payload ratio is very low. Fuel ratio in total rocket mass before the launch reaches about 90%. Payload ratio is just several percents. And rockets of this type need complex components such as a burner and turbopumps but are wasted after used once. Recently, as a launch method resolving these problems beamed energy propulsion (BEP) attends attraction.

In BEP a thruster is supplied beamed energy from outside of the thruster such as ground based beam sources and converts the energy to thrust. BEP thruster doesn't have to contain fuel. In a high density atmosphere air breathing system can be used. BEP thruster installed the system can use the air as propellant. High payload ratio can be realized. Air breathing system requires only nozzles and valves and doesn't need complex components. Because of high payload ratio and simple system low cost space launcher and spreading of space utilization are expected.

1.2 Energy source of BEP

In BEP research, a method to use a laser as an energy source has been main stream.[1] Kantrowitz[2] first suggested BEP using the laser beamed from facilities on the ground or in the space in 1972. Around the same time Raizer et al[3] figured out a laser energy conversion process as Laser Supported Combustion (LSC) and Laser Supported Detonation (LSD). In 1998 Myrabo[4,5] et al. demonstrated flight test with Lightcraft and a CO_2 pulse laser.

The laser travels straight with low diffusion. BEP requiring long distance transmission needs features of the laser. But BEP asks large output of an energy source. Current laser sources can't make an output to be able to apply BEP. On the other hand, a microwave has already realized 1MW beam sources. Microwave beam sources are being developed as heat source of nuclear fusion. A microwave source which has an output to be able to apply BEP will be realized in not so distant future. Diffusion can be resolved with high frequency.

Using 1MW gyrotron[6-8] of microwave source our research group develops Microwave Rocket.[9-17]

1.3 Thrust generation model of Microwave Rocket

Microwave beamed to a focusing reflector causes a breakdown of air and generates plasma at the focal point. The ionization front propagates toward a beam source

absorbing microwave energy. The propagation velocity of the ionization front increases with the microwave power density. When the ionization front propagates at the transonic or supersonic speed, it drives a shock wave in front of it.

A thrust generation model of Microwave Rocket has been proposed based on a pulse detonation engine (PDE) model. A cylindrical body has a closed end and an open end. The closed end is called a thrust wall. In PDEs, combustion in a thruster drives a shock wave and pressure at the thrust wall is maintained higher than ambient/initial pressure during the period from the ignition at the thrust wall to the arrival of an expansion wave coming back from the open end.[18,19] In the Microwave Rocket model, the combustion is replaced by microwave heating. Figure 1.1 shows the Microwave Rocket engine cycle. An impulse gained during a cycle is equal to a product of the pressure kept at the thrust wall and the period from the ignition to the arrival of the expansion wave. This cycle is repeated and Microwave Rocket generates thrust intermittently.

1.4 Past research of Microwave Rocket in our research group

First, flight experiments were conducted with a single microwave pulse. Flight passes of the thruster along to altitude direction were measured by a laser displacement gauge. Impulses were calculated from initial velocity of the thruster. We estimated performance of Microwave rocket using impulses I and momentum coupling coefficients C_m defined as a ratio of impulses to input energy of the microwave was estimated. In these experiments I and C_m dependences on microwave power, thruster length and width of a microwave pulse were figured out. Flight experiments with multi microwave pulses were conducted too. Impulses gaining from 2nd pulse decrease to 50-60% of Impulses gaining from 1st pulse. The cause that impulses decrease was thought to be changing conditions inside of the thruster by 1st pulse. It was suggested to exhaust the high temperature gas remaining in the thruster by front air breathing.

To install air breathing system and to observe inside of the thruster, thrust measurement using fixed thruster was required. Two pressure gauges were mounted near the thrust wall and the open end of the fixed thruster. Impulses were estimated from pressure history at the thrust wall with PDE model and well agreed with results of flight experiments. Thrust estimation of the fixed thruster was enabled.

Synflex tubes connect high pressure tank and the thrust wall side of the thruster. High pressure generates a flow in the thruster as an air breathing thruster. The flow exhausts high temperature gas and improves impulses obtained by microwave pulses since the second. Therefore 1sec endurance operations were conducted successfully.

Thrust measurements by pressure history make observation in the thruster possible too. Propagation velocities of the shockwave U_{shock} and the expansion wave a_3 were measured from differences between arrival times of each wave. A high speed camera captured propagation velocities of the ionization front U_{ioniz}. U_{shock} and U_{ioniz} increase with the peak microwave power density S_0 as shown in Figure 1.2. In the low S_0 region U_{shock} was larger than U_{ioniz} and the shock wave and the ionization front had separated. It can not be explained with theory of detonation wave called ZND model. In addition it is difficult to capture distributions of parameters along thruster longitudinal direction.

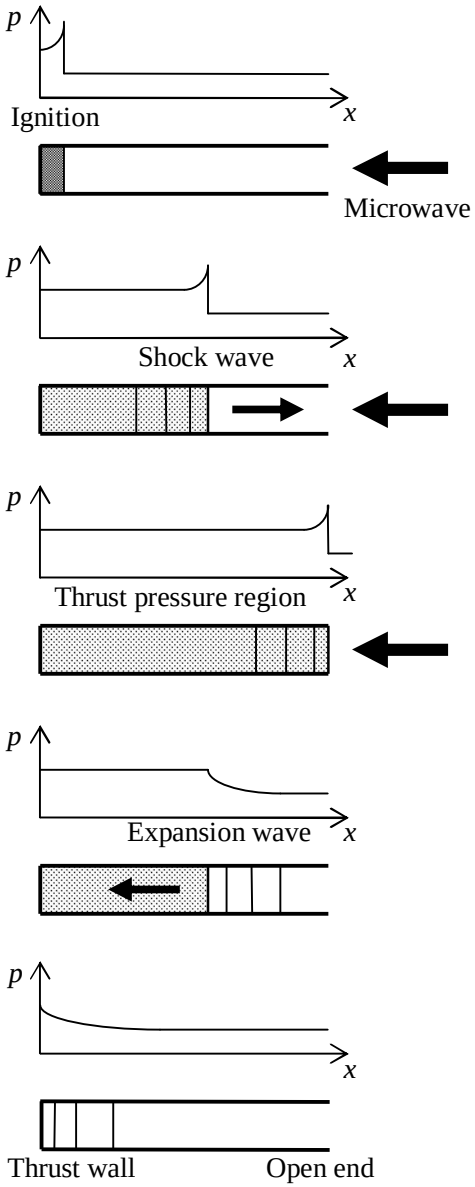

FIGURE 1.1. Schematics of the pressure distribution evolution along the longitudinal direction

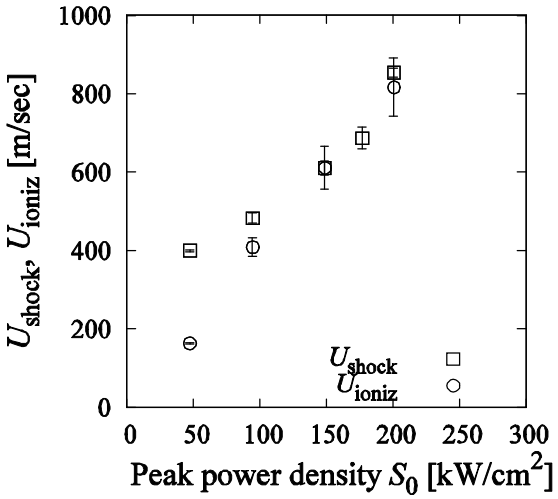

FIGURE 1.2. Dependence of U_{shock} and U_{ioniz} on S_0

1.5 Objects of this research

For design optimization and for flight trajectory analysis, energy conversion model is required. In this research Using measured the ionization front velocity U_{ioniz} CFD simulation was performed. This simulation method doesn't need to assume any specific heat constant for microwave heating process. CFD results can be validated with U_{shock}, p3 and a3. Validated results can provide distributions of parameters along thruster longitudinal direction. Theoretical model of energy conversion process of Microwave Rocket was suggested. Comparing the model with ZND detonation model, difference of each model was mentioned.

Chapter 2

CFD methods

2.1 The governing equations of flow fields

Governing equations of fluid flow consist of three conservation equations and an equation of state. The conservation equations are mass, momentum and energy conservation equations. Because the conservation equations have four unknowns the equation of state is introduced to close the system of the governing equations.[20]

The Navier-Stokes equations are generally accepted as an adequate description for aerodynamic flows at standard conditions. Using index notation, we can write them as

$$\frac{\partial \rho}{\partial t} + \frac{\partial \rho u_j}{\partial x_j} = 0 \qquad (2.1)$$

$$\frac{\partial \rho u_i}{\partial t} + \frac{\partial}{\partial x_j}\left(\rho u_i u_j + p\delta_{ij} + \tau_{ij}\right) = 0 \qquad (2.2)$$

$$\frac{\partial E}{\partial t} + \frac{\partial}{\partial x_j}\left((E + p)u_j + \tau_{ij}u_i + q_j\right) = 0 \qquad (2.3)$$

Where ρ is the density (mass per unit volume), ρu_i is the momentum per unit volume in the x_i direction and E is the energy per unit volume. p is the pressure which is a known function of the internal energy e and the density. For a perfect gas, the pressure has the form

$$p = \rho RT = (\gamma - 1)\rho e, \quad e = \frac{E}{\rho} - \frac{1}{2}u_i^2 \qquad (2.4)$$

where $\gamma = c_p/c_v$ is the ratio of specific heats, T is the temperature and R is the gas constant. For a calorically perfect gas $e = c_v T$. Then

$$E = \rho e + \frac{1}{2}\rho u_i^2 = \rho c_v T + \frac{1}{2}\rho u_i^2 \qquad (2.5)$$

For the Nanier-Stokes equations, the shear stresses are proportional to first derivatives of the velocities.

$$\tau_{ij} = -\mu\left(\frac{\partial u_i}{\partial x_j} + \frac{\partial u_j}{\partial x_i}\right) - \lambda\frac{\partial u_k}{\partial x_k}\delta_{ij} \qquad (2.6)$$

where m and λ are the first and second coefficients of viscosity ($\lambda = -2/3\mu$ for most fluids). The heat conduction is proportional to temperature gradients

$$q_j = -\kappa\frac{\partial T}{\partial x_i} \qquad (2.7)$$

where the conductivity κ is related to the viscosity through the Prandtl number $Pr = c_v\mu/\kappa$. Pr is nearly constant for most conditions.

For flows with negligible viscous and thermal conduction effects, we can write the governing equations forming the Euler equations as

$$\frac{\partial \rho}{\partial t} + \frac{\partial \rho u_j}{\partial x_j} = 0 \tag{2.8}$$

$$\frac{\partial \rho u_i}{\partial t} + \frac{\partial}{\partial x_j}\left(\rho u_i u_j + p\delta_{ij}\right) = 0 \tag{2.9}$$

$$\frac{\partial E}{\partial t} + \frac{\partial}{\partial x_j}\left((E+p)u_j\right) = 0 \tag{2.10}$$

where the variables have the same definitions as the Navier-Stokes equations.
For medium to high Reynolds number flows, the inviscid terms dominate and the Euler equations are used in this research.

The governing equations are said to be in conservation law form or more precisely in divergence law form, if they are written as follows.

$$\frac{\partial \boldsymbol{U}}{\partial t} + \nabla \cdot \boldsymbol{F} = \boldsymbol{W} \tag{2.11}$$

where $\boldsymbol{U}$ is the vector of conserved quantities, $\boldsymbol{\nabla}$ is the divergence operator and $\boldsymbol{F}$ is the flux vector. If the system is conservative (no source of mass, momentum or energy), the source term $\boldsymbol{W}$ is zero. In this research, to calculate an effect of heat addition from microwave absorption by plasma generated behind the ionization front, an energy source term w is given to an energy conservation equation. One dimensional Euler equations used in this research, the vector of conserved quantities, the flux vector and the source vector are

$$\frac{\partial \boldsymbol{U}}{\partial t} + \frac{\partial \boldsymbol{F}}{\partial x} = \boldsymbol{W} \tag{2.12}$$

$$\boldsymbol{U} = \begin{pmatrix} \rho \\ \rho u \\ E \end{pmatrix}, \quad \boldsymbol{F} = \begin{pmatrix} \rho u \\ \rho u^2 + p \\ (E+p)u \end{pmatrix}, \quad \boldsymbol{W} = \begin{pmatrix} 0 \\ 0 \\ w \end{pmatrix} \tag{2.13}$$

2.2 Jacobians

We can write the conservation equation in non-conservation form as

$$\frac{\partial \boldsymbol{U}}{\partial t} + \frac{\partial \boldsymbol{F}}{\partial x} = \boldsymbol{W} \tag{2.14}$$

$$\frac{\partial \boldsymbol{U}}{\partial t} + \frac{\partial \boldsymbol{F}}{\partial \boldsymbol{U}}\frac{\partial \boldsymbol{U}}{\partial x} = \boldsymbol{W} \tag{2.15}$$

$$\frac{\partial \boldsymbol{U}}{\partial t} + \boldsymbol{A}\frac{\partial \boldsymbol{U}}{\partial x} = \boldsymbol{W} \tag{2.16}$$

where $\boldsymbol{A} = \dfrac{\partial \boldsymbol{F}}{\partial \boldsymbol{U}}$

The matrics $\boldsymbol{A}$ is called Jacobian of $\boldsymbol{F}$ with respect to $\boldsymbol{U}$. In general, for m dimensional vectors $\boldsymbol{U}$ and $\boldsymbol{F}$

$$\boldsymbol{A}=\frac{\partial \boldsymbol{F}}{\partial \boldsymbol{U}}=\begin{pmatrix} \frac{\partial f_1}{\partial u_1} & \frac{\partial f_1}{\partial u_2} & \cdots & \frac{\partial f_1}{\partial u_m} \\ \frac{\partial f_2}{\partial u_1} & \frac{\partial f_2}{\partial u_2} & \cdots & \frac{\partial f_2}{\partial u_m} \\ \vdots & \vdots & \ddots & \vdots \\ \frac{\partial f_m}{\partial u_1} & \frac{\partial f_m}{\partial u_2} & \cdots & \frac{\partial f_m}{\partial u_m} \end{pmatrix} \tag{2.17}$$

If $\boldsymbol{U}$ can be defined in terms of vector $\boldsymbol{V}$

$$\boldsymbol{U}=(\boldsymbol{V}),\ \ \boldsymbol{T}=\frac{\partial \boldsymbol{U}}{\partial \boldsymbol{V}} \tag{2.18}$$

where the matrix $\boldsymbol{T}$ is Jacobian of $\boldsymbol{U}$ with respect to $\boldsymbol{V}$. Then we can also the non-conservative form as

$$\boldsymbol{T}\frac{\partial \boldsymbol{V}}{\partial t}+\boldsymbol{A}\boldsymbol{T}\frac{\partial \boldsymbol{V}}{\partial x}=\boldsymbol{W} \tag{2.19}$$

$$\frac{\partial \boldsymbol{V}}{\partial t}+\boldsymbol{A}'\frac{\partial \boldsymbol{V}}{\partial x}=\boldsymbol{W}' \tag{2.20}$$

where $\boldsymbol{A}'=\boldsymbol{T}^{-1}\boldsymbol{A}\boldsymbol{T}$ and $\boldsymbol{W}'=\boldsymbol{T}^{-1}\boldsymbol{W}$.

The matrix $\boldsymbol{T}^{-1}$ is Jacobian of $\boldsymbol{V}$ with respect to $\boldsymbol{U}$. It is needless to invert $\boldsymbol{T}$. Choosing simple $\boldsymbol{V}$, it is also easy to find Jacobians with respect to $\boldsymbol{U}$ with following form

$$\frac{\partial}{\partial \boldsymbol{U}}=\frac{\partial}{\partial \boldsymbol{V}}\frac{\partial \boldsymbol{V}}{\partial \boldsymbol{U}}=\frac{\partial}{\partial \boldsymbol{V}}\boldsymbol{T}^{-1} \tag{2.21}$$

2.3 Steger Warming Flux Vector Splitting (FVS)

The early special differencing schemes did not correctly account for a transport of information according to a direction of the characteristics. Physical information is transported from upwind to leeward. To correct differencing direction, upwind special differencing scheme is useful but its application to multidimensional problem was difficult.

The Steger Warming approach is to split the flux vectors into positively-moving and negatively-moving components. The Euler flux vectors are homogeneous in the vector of conserved quantities. That is

$$\boldsymbol{F}(\lambda \boldsymbol{U})=\lambda \boldsymbol{F}(\boldsymbol{U}) \tag{2.22}$$

where λ is a constant scalar. This implicates that the flux vectors can be written as the product of the Jacobian matrix and the vector of conserved quantities.

$$\boldsymbol{F}=\frac{\partial \boldsymbol{F}}{\partial \boldsymbol{U}}\boldsymbol{U}=\boldsymbol{A}\boldsymbol{U} \tag{2.23}$$

To split the flux vectors we need to diagonalize the Jacobian matrix $\boldsymbol{A}$. As shown in the former, it is difficult and complicated to find eigenvalues and eigenvectors directly. It is easy to do the diagonalization using a different set of variables and then transform back to the vector of primitive variables $\boldsymbol{V}=(\rho, u, p)^t$. Then we can write the Jacobian matrix $\boldsymbol{A}$ in terms of the transformations from $\boldsymbol{U}$ to $\boldsymbol{V}$ and the Jacobian matrix of $\boldsymbol{F}$ with respect to $\boldsymbol{V}$.

$$\boldsymbol{A} = \frac{\partial \boldsymbol{F}}{\partial \boldsymbol{U}} = \frac{\partial \boldsymbol{U}}{\partial \boldsymbol{V}} \frac{\partial \boldsymbol{V}}{\partial \boldsymbol{U}} \frac{\partial \boldsymbol{F}}{\partial \boldsymbol{V}} \frac{\partial \boldsymbol{V}}{\partial \boldsymbol{U}} \tag{2.24}$$

To compute the Jacobian matrixes, $\boldsymbol{F}$ and $\boldsymbol{U}$ have to be expressed in variables of $\boldsymbol{V}$ and $\boldsymbol{V}$ have to be expressed in variables of $\boldsymbol{U}$. Changing expression can be performed with relations

$$p = (\gamma - 1)\left(E - \frac{1}{2\rho}(\rho u)^2 \right) \tag{2.25}$$

$$E = \frac{p}{\gamma - 1} + \frac{1}{2}\rho u^2 \tag{2.26}$$

Then the vectors are written as

$$\boldsymbol{F} = \begin{pmatrix} \rho u \\ \rho u^2 + p \\ (E + p)u \end{pmatrix} = \begin{pmatrix} \rho u \\ \rho u^2 + p \\ \dfrac{\gamma}{\gamma - 1} pu + \dfrac{\rho u^3}{2} \end{pmatrix} \tag{2.27}$$

$$\boldsymbol{U} = \begin{pmatrix} \rho \\ \rho u \\ E \end{pmatrix} = \begin{pmatrix} \rho \\ \rho u \\ \dfrac{p}{\gamma - 1} + \dfrac{\rho u^2}{2} \end{pmatrix} \tag{2.28}$$

$$\boldsymbol{V} = \begin{pmatrix} \rho \\ u \\ p \end{pmatrix} = \begin{pmatrix} \rho \\ \dfrac{\rho}{\rho u} \\ (\gamma - 1)\left\{ E - \dfrac{(\rho u)^2}{2\rho} \right\} \end{pmatrix} \tag{2.29}$$

and the Jacobians matrixes are

$$\frac{\partial \boldsymbol{F}}{\partial \boldsymbol{V}} = \begin{pmatrix} u & \rho & 0 \\ u^2 & 2\rho u & 1 \\ \dfrac{u^2}{2} & \dfrac{\gamma}{\gamma - 1} p + \dfrac{3}{2}\rho u^2 & \dfrac{\gamma}{\gamma - 1} u \end{pmatrix} \tag{2.30}$$

$$\boldsymbol{S} = \frac{\partial \boldsymbol{V}}{\partial \boldsymbol{U}} = \begin{pmatrix} 1 & 0 & 0 \\ -\dfrac{\rho u}{\rho^2} & \dfrac{1}{\rho} & 0 \\ (\gamma - 1)\dfrac{(\rho u)^2}{2\rho^2} & -(\gamma - 1)\dfrac{\rho u}{\rho} & \gamma - 1 \end{pmatrix} = \begin{pmatrix} 1 & 0 & 0 \\ -\dfrac{u}{\rho} & \dfrac{1}{\rho} & 0 \\ (\gamma - 1)\dfrac{u^2}{2} & -(\gamma - 1)u & \gamma - 1 \end{pmatrix} \tag{2.31}$$

$$\boldsymbol{S}^{-1}=\frac{\partial \boldsymbol{U}}{\partial \boldsymbol{V}}=\begin{pmatrix} 1 & 0 & 0 \\ u & \rho & 0 \\ \frac{u^2}{2} & \rho u & \frac{1}{\gamma-1} \end{pmatrix} \tag{2.32}$$

The matrix $\frac{\partial \boldsymbol{F}}{\partial \boldsymbol{V}}$ has complex form, but a product of the matrixes $\frac{\partial \boldsymbol{F}}{\partial \boldsymbol{V}}$ and $\frac{\partial \boldsymbol{V}}{\partial \boldsymbol{U}}$ is easy to diagonalize.

$$\frac{\partial \boldsymbol{V}}{\partial \boldsymbol{U}}\frac{\partial \boldsymbol{F}}{\partial \boldsymbol{V}}=\begin{pmatrix} u & \rho & 0 \\ 0 & u & 1/\rho \\ 0 & \rho a^2 & u \end{pmatrix} \tag{2.33}$$

Where $a^2=\gamma RT=\gamma p/\rho$.

To diagonalize this matrix product, we can easily find eigenvalues λ and eigenvectors $\boldsymbol{v}$. When $\lambda=u$

$$\boldsymbol{v}_1=t_1\begin{pmatrix} 1 \\ 0 \\ 0 \end{pmatrix} \tag{2.34}$$

when $\lambda=u+a$

$$\boldsymbol{v}_2=t_2\begin{pmatrix} \rho \\ a \\ \rho a^2 \end{pmatrix} \tag{2.35}$$

when $\lambda=u+a$

$$\boldsymbol{v}_3=t_3\begin{pmatrix} \rho \\ -a \\ \rho a^2 \end{pmatrix} \tag{2.36}$$

where t_1, t_2 and t_3 are arbitrary constants.

Using these values and vectors, an eigenvalue matrix $\boldsymbol{\Lambda}$, a right eigenvector matrix $\boldsymbol{C}$ and a left eigenvector matrix $\boldsymbol{C}^{-1}$ are formed.

$$\boldsymbol{\Lambda}=\begin{pmatrix} u & 0 & 0 \\ 0 & u+a & 0 \\ 0 & 0 & u-a \end{pmatrix} \tag{2.37}$$

$$\boldsymbol{C}=\begin{pmatrix} 1 & 0 & -\frac{1}{a^2} \\ 0 & \frac{1}{2a} & \frac{1}{2\rho a^2} \\ 0 & -\frac{1}{2a} & \frac{1}{2\rho a^2} \end{pmatrix} \tag{2.38}$$

$$\boldsymbol{C}^{-1}=\begin{pmatrix}1 & \rho & \rho\\ 0 & a & -a\\ 0 & \rho a^2 & \rho a^2\end{pmatrix} \tag{2.39}$$

Then the Jacobian matrix of $\boldsymbol{F}$ with respect to $\boldsymbol{U}$ may be written as

$$\boldsymbol{A}=\frac{\partial \boldsymbol{F}}{\partial \boldsymbol{U}}=\boldsymbol{S}^{-1}\boldsymbol{C}^{-1}\boldsymbol{\Lambda}\boldsymbol{C}\boldsymbol{S} \tag{2.40}$$

The actual flux vector splitting is done by dividing the flux into two part: that due to the positive eigenvalues, and that due to the negative eigenvalues.

$$\boldsymbol{F}=\boldsymbol{F}_{+}+\boldsymbol{F}_{-} \tag{2.41}$$

$$\boldsymbol{F}_{+}=\boldsymbol{A}_{+}\boldsymbol{U}=\boldsymbol{S}^{-1}\boldsymbol{C}^{-1}\boldsymbol{\Lambda}_{+}\boldsymbol{C}\boldsymbol{S}\boldsymbol{U} \tag{2.42}$$

$$\boldsymbol{F}_{-}=\boldsymbol{A}_{-}\boldsymbol{U}=\boldsymbol{S}^{-1}\boldsymbol{C}^{-1}\boldsymbol{\Lambda}_{-}\boldsymbol{C}\boldsymbol{S}\boldsymbol{U} \tag{2.43}$$

where $\boldsymbol{\Lambda}_{\pm}$ are the diagonal matrixes of the positive and negative eigenvalues. One way of writing these matrixes is

$$\boldsymbol{\Lambda}_{+}=\begin{pmatrix}\frac{1}{2}\left(u+|u|\right) & 0 & 0\\ 0 & \frac{1}{2}\left(u+a+|u+a|\right) & 0\\ 0 & 0 & \frac{1}{2}\left(u-a+|u-a|\right)\end{pmatrix} \tag{2.44}$$

$$\boldsymbol{\Lambda}_{-}=\begin{pmatrix}\frac{1}{2}\left(u-|u|\right) & 0 & 0\\ 0 & \frac{1}{2}\left(u+a-|u+a|\right) & 0\\ 0 & 0 & \frac{1}{2}\left(u-a-|u-a|\right)\end{pmatrix} \tag{2.45}$$

Computing with this way, positive terms of $\boldsymbol{\Lambda}_{+}$ don't change but negative terms of $\boldsymbol{\Lambda}_{+}$ become zero and positive terms of $\boldsymbol{\Lambda}_{-}$ become zero but negative terms of $\boldsymbol{\Lambda}_{+}$ don't change automatically. To write codes this calculation doesn't need conditional branch sentence and can computes fast.

Stored data is about the conserved quantities vector $\boldsymbol{U}$ at cell centroid points. The flux vectors $\boldsymbol{F}$ at cell surfaces depend on the values of the stored data at the neighboring points. If we use a simple average across the cell, then we get a central difference representation of the spatial derivatives. But information of flow fields travels from upwind to leeward. With this FVS scheme, we have found $\boldsymbol{F}_{+}$ which is moving in the positive x direction due to positive eigenvalues and $\boldsymbol{F}_{-}$ which is moving in the negative x direction due to negative eigenvalues. To extrapolate the fluxes from stored data at the upwind cellcentroid points Steger and Warming used the following form

$$\begin{aligned}\boldsymbol{F}_{i+1/2}&=\boldsymbol{F}_{+,i}+\boldsymbol{F}_{-,i+1}\\ &=\boldsymbol{A}_{+,i}\boldsymbol{U}_{i}+\boldsymbol{A}_{-,i+1}\boldsymbol{U}_{i+1}\end{aligned} \tag{2.46}$$

because the positively moving flux should use the stored data from the left of the cell face and the negatively moving flux should come from the right.

A more recent approach is to evaluate the Jacobian matrixes $\boldsymbol{A}_{\pm}$ at the same

location using averaged variables. In this case we have

$$\begin{aligned} \boldsymbol{F}_{i+1/2} &= \boldsymbol{F}_{+,i} + \boldsymbol{F}_{-,i+1} \\ &= \boldsymbol{A}_{+,i+1/2}\boldsymbol{U}_i + \boldsymbol{A}_{-,i+1/2}\boldsymbol{U}_{i+1} \end{aligned} \tag{2.47}$$

$$\boldsymbol{A}_{\pm,i+1/2} = \boldsymbol{A}_{\pm}\left(\frac{1}{2}\left(\boldsymbol{U}_i + \boldsymbol{U}_{i+1}\right)\right)$$

The approach evaluating the Jacobians at the same location is much less dissipative than the pure Steger Warming flux vector splitting. The result is that the latter method gives much more realistic boundary layer profiles, thus it is preferred. In this research using the letter method, flux vectors were evaluated.

The convection term of the governing equations were evaluated with the flux vecters and following form

$$\frac{\partial \boldsymbol{F}}{\partial x} \cong \frac{\boldsymbol{F}_{i+1/2} - \boldsymbol{F}_{i-1/2}}{\Delta x} \tag{2.48}$$

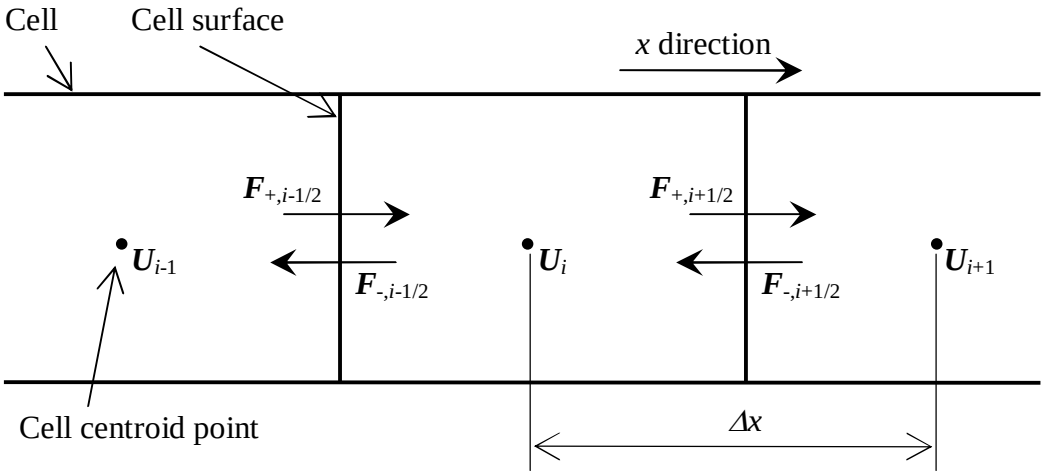

FIGURE 2.1. Locations where vectors are evaluated

2.4 Explicit time advancement

Because the temporal direction of the governing equations is hyperbolic, we can use a backward difference for an explicit method. We evaluate the right hand side of the above equation at the current time level and extrapolate forward in time. For simplicity, a simple ordinary differential equation will be considered.

$$\frac{\partial y}{\partial t} = f\left(y\right) \tag{2.49}$$

An explicit time advance scheme is

$$\frac{y^{n+1} - y^n}{\Delta t} = f\left(y^n\right) \tag{2.50}$$

$$y^{n+1} = y^n + \Delta t f\left(y^n\right) \tag{2.51}$$

where the superscript denotes the time level of the computation. By convention the time level n is the current time level where we know the solution (from the initial conditions of from a previous time step) and n+1 is the unknown future time level.

Runge-Kutta method was used as a time advancement in this research. Setting other steps between time steps, this method obtains stability and accuracy of the solution. For example, to use two-order scheme

$$y^{(1)} = y^n + \frac{1}{2}\Delta t f\left(y^n\right) \tag{2.52}$$

$$y^{n+1} = y^n + \Delta t f\left(y^{(1)}\right) \tag{2.53}$$

we can evaluate change in the solution from time level n to n+1 more actually. General extension of this method as shown below is a kth-order Runge-Kutta method.

$$\begin{cases} y^{(1)} = y^n + \lambda_1 \Delta t f\left(y^n\right) \\ y^{(i)} = y^n + \lambda_i \Delta t f\left(y^{(i-1)}\right) \\ \quad \vdots \\ y^{(k)} = y^n + \lambda_k \Delta t f\left(y^{(k-1)}\right) \\ y^{n+1} = y^{(k)} \end{cases}, \quad \lambda_i = \frac{1}{k-i+1} \tag{2.54}$$

It is said that fourth-order Runge-Kutta method is well stable. This method is used in this research.

2.5 CFL number

The time step Δt is chosen to keep the solution stable. Numerically, information is spread at the rate of $\Delta x/\Delta t$. On the other hand, the propagation velocity of a physical signal is $|u|+a$. If $\Delta x/\Delta t$ is smaller than $|u|+a$, sufficient information to decide the physical state of the following time step can't be acquired in the scheme, and a calculation solution will be emitted. So, it is easy to show that the one-dimensional Euler equations are stable for time steps thst satisfy the following relation.

$$\Delta t \le \frac{\Delta x}{|u|+a} \Leftrightarrow |u|+a \le \frac{\Delta x}{\Delta t} \tag{2.55}$$

In practice, usually some fraction ν called the CFL number of the limiting time step is taken

$$\Delta t = \nu \Delta t_{\max} = \nu \frac{\Delta x}{|u|+a} \tag{2.56}$$

It is called for that the CFL number is 1 or less for $\Delta x/\Delta t$ not to exdeed $|u|+a$. However, also when the number is extremely smaller than 1, a difference arises in the propagation velocity of numerical information and a physical signal, and a calculation solution becomes blunt. Therefore, the CFL number doesn't exceed 1 but its value near 1 is desirable. In this research the CFL number ν is 0.5

This method is viable and works well. But, there is a limitation: the time step is proportional to the mesh spacing. Thus, if the grid is refined to capture some physical feature of the flowfield, the time step must also be reduced. Then, if there is some physical time that the solution must be advanced, then the computational time will increase in proportion to the amount of grid refinement.

2.6 Microwave heating

The absorbed power density of the microwave is given by ηS_{average}[kW/cm^2]. S_{average} is power density computed from the following equation from the total output power of microwave P, and the thruster cross-section area A.

$$S_{\text{average}} = \frac{P}{A} \qquad (2.57)$$

However, in observation of an ionization front with a high-speed camera, luminescence of plasma is observed not the whole thruster but in the plasma column as shown in a FIGURE 2.2.

Since microwave is absorbed by plasma, only the component which entered into this plasma column among the outputted microwave will be absorbed. Therefore, ratio of the absorbed component to the total output of microwave is necessary to take into consideration. The power density distribution to a direction perpendicular to the propagation direction of the microwave used by this research is the Gaussian distribution of the beam waist 20.4 [mm] as shown in FIGURE 2.2. The ratio of the integration value of the range which enters into the plasma column of this distribution, and a total output is set to η.

Heating by microwave assumed that it was made equally in the region which have thickness λ and makes an ionization front a head. Moreover, the wavelength of microwave is assumed to λ. Therefore, the source term w in the energy equation of governing equations is as follows.

$$w = \frac{\eta S_{\text{average}}}{\lambda} \qquad \text{(in a heating region)} \qquad (2.58)$$

$$w = 0 \qquad \text{(not in a heating region)} \qquad (2.59)$$

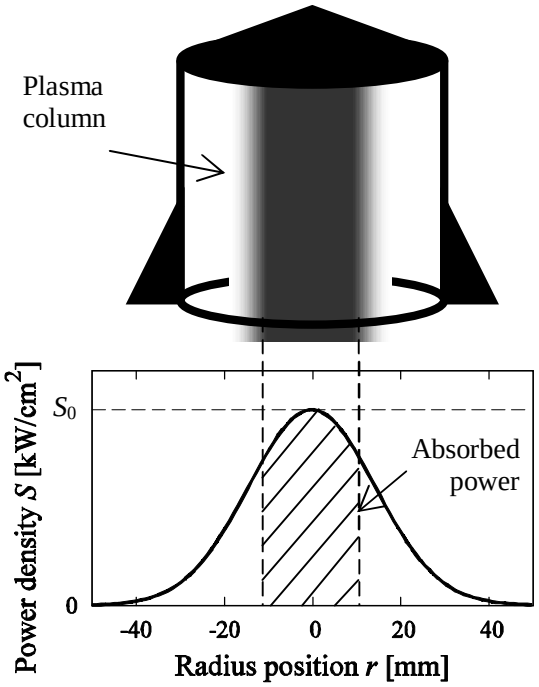

FIGURE 2.2. Plasma column and radius distribution of microwave power density

2.7 Computational conditions

As shown in FIGURE 2.3, 6000 grids have been arranged at regular intervals, and a 300mm length thruster was simulated. The x-axis was placed in the thruster longitudinal direction, x=0 was used as the thrust wall and x=0.3 [m] was made into the open end.
The heating region is determined from the propagating speed of the ionization front U_{ioniz}, and thickness of the heating region λ.

$$U_{\mathrm{ioniz}}t-\lambda \le x \le U_{\mathrm{ioniz}}t \qquad (2.60)$$

t is the lapsed time from the time t_0 when ignition by a dielectric breakdown is made in the thrust wall with the oscillation start of microwave. λ is assumed wave length of microwave and U_{ioniz} is obtained with following empirical equation.

$$U_{\mathrm{ioniz}} = 3.4S_0 + 41.9 \qquad (2.61)$$

Past experimental data shown in FIGURE 1.2 gives this equation.

Boundary conditions are used these relations:

Thrust wall side:

- Flow velocity is zero.
- The gradients of the other parameters are zero

Open end side:

- Static pressure is constant.
- The gradients of the other parameters are zero

Electromagnetic fields and plasma interaction are not solved in this method. It's very simplified method.

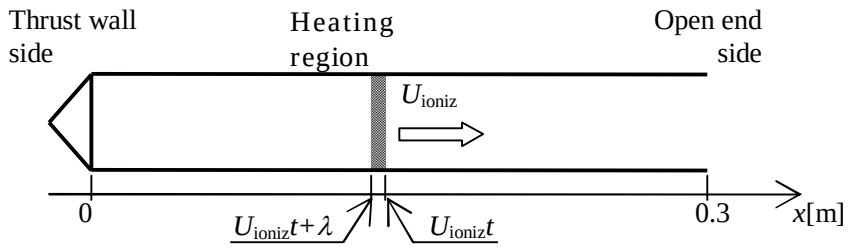

FIGURE 2.3. Computational area

2.8 Grid convergence study

In the flow field which the microwave supported detonation wave propagates, the most rapid change arising in the heating region, this region needs the finest grid resolution.
Then, t_{plateau} was evaluated for every number of the grids arranged within the heating region λ/dx, and grid resolution was verified. Distribution of t_{plateau} for every number of grids in S_0=120[kW/cm^2] and S_0=320[kW/cm^2] is shown in FIGURE 2.4.

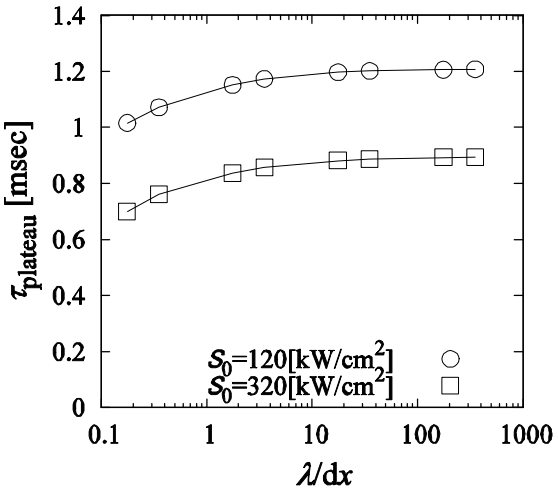

FIGURE 2.4. Grid convergence

Results of $t_{plateau}$ converge enough where λ/dx is higher than 10. CFD was performed with λ/dx 35. This resolution corresponds to dx=5.0e-5[m] and 6000grids in 0.3[m] long.

2.9 Verification of CFD results

Using the above method and conditions one-dimensional numerical simulation of the flow field in the Microwave Rocket which the microwave supported detonation wave propagates was conducted. The results of numerical analysis and experiments were compared about the pressure p_3 and sound speed a_3 in the trust pressure region, and the validity of the numerical analysis results was verified. Distribution of the pressure p_3 and sound speed a_3 at given power density S_0 are shown in FIGURE 2.5, 2.6, respectively.

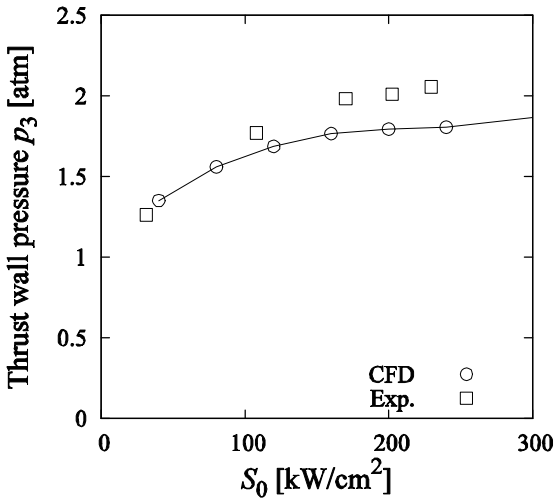

FIGURE 2.5. Comparison of p_3

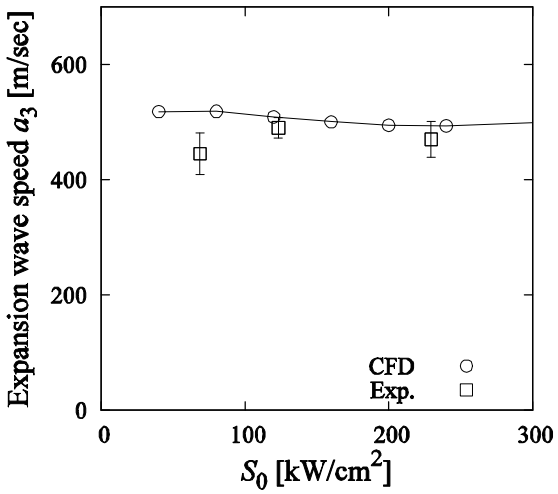

FIGURE 2.6. Comparison of a_3

The magnitude and tendency of the numerical analysis result of p_3 and a_3 are well agreed with the experimental result good. The very simplified method, using the measured propagation velocity of ionization front and assuming the wavelength of microwave to absorption region width, enabled observation of the changes of the state by the microwave supported detonation wave.

Chapter 3

Structure of a microwave supported detonation wave

Distribution along the thruster longitudinal direction of the pressure p and temperature T in the thruster generated by heating to the ionization front by microwave can be categorized into three regimes according to the power density of microwave S_0. Three distribution form are called a microwave supported combustion (MSC) regime in $S_0 <$ 136[kW/cm^2], a transition regime in $136 \leqq S_0 \leqq 238$[kW/cm^2] and a microwave supported detonation (MSD) regime in $S_0 \geqq 238$[kW/cm^2] respectively. Pressure and temperature distribution along the thruster longitudinal direction with S_0=100[kW/cm^2] in the MSC regime is shown in FIGURE 3.1, that with S_0=200[kW/cm^2] in the transition regime is shown in FIGURE 3.2 and that with S_0=300[kW/cm^2] in the MSD regime is shown in FIGURE 3.3.

The horizontal axis of FIGURE 3.1-3.3 shows the position of the thruster longitudinal direction, x= 0 expresses the thrust wall and x= 0.3 expresses the open end. All the calculation area from the thrust wall to the open end were shown in the left-hand side of the figures, expanding the horizontal axis to shows the heating region distributions are shown in the right-hand side. Time t[msec] expressed the lapsed time from time t_0 when the ignition occurred at the thrust wall, and three distribution (a) (b) (c) in different time are shown every S_0. And the dotted line showed the heating region obtained by the lapsed time t and U_{ioniz} which is found with the empirical equation (2.61).

3.1 MSC regime

In the MSC regime as shown in FIGURE 3.1, two steps propagate toward the thruster exit from the thrust wall with time. The heating region given from the empirical equation (2.61) is equivalent to the left-hand side step, and the right-hand side step is the shock wave preceded with the heating region. The heating region and the shock wave propagate at the fixed speed U_{shock} and U_{ioniz} from the thrust wall, and the distance of two steps expands gradually.

3.2 Transition regime

Also in the case of Transition regime as power density gone up and shown in FIGURE 3.2, two steps propagate. The heating region is equivalent to the step of the left-hand side behind the propagation direction like the case of MSC regime, and the front step is a proceeding shock wave. However, the thrust pressure region does not continue from immediately after the left-hand side step, but it differs from the MSC regime in that a slope is in between. Since the propagating speed difference of the shock wave and the

ionization front becomes small compared with the MSC regime in the transition regime as shown in FIGURE 3.2, the distance of the proceeding shock wave and the heating region narrows.

3.3 MSD regime

Power density goes up further, in the MSD regime as shown in FIGURE 3.3, One step of pressure and temperature distribution precedes, and a plateau region and a slope propagate behind the step. The heating region is equivalent to the step to proceed.

3.4 Rayleigh flow

In MSC regime and Transition regime, the state that the open air pressure ahead of a shock wave was maintained is set with a state 1, the state of being maintained between the shock wave and the heating region is set with a state 2 and the state of the thrust pressure region behind the heating region or the slope is set with a state 3. The density, flow velocity, pressure and temperature of each state are expressed using a subscript. Moreover, in the transition regime, the state between the heating region and the slope is set with a state 2.5. In MSD regime, the state ahead of a heating region is set with a state 1, the state of being maintained between the heating region and the slope is set with a state 2. The state of the thrust pressure region behind a slope is set with a state 3.

In all the regimes, the temperature rise is yielded in the heating region, and this region can be treated as a control volume with heating as shown in the graph to which the heating region was expanded. That is, it turns out that the Rayleigh flow relation which is an analytical solution of the one-dimensional regular flow with heating is applicable to the change of the state in the heating region.

3.5 Rarefaction wave

Next, the propagation Mach number into the partial flow velocity of a tail of the heating region and a head of the thrust pressure region are set to M_a and M_b respectively. The distribution of these propagation Mach numbers at every given power density S_0 is shown in FIGURE 3.4. In the MSC regime, since the tail of a heating region and the head of the thrust pressure region touch, so $M_a=M_b$. In the transition regime, although the slope is between the tail of the heating region, and the head of the thrust pressure region, it becomes $M_a=M_b$. And the value is constant at $M_a=M_b=1$. That is, it was confirmed that the slope in the pressure and temperature distribution in the transition regime shown in FIGURE 3.2 is a rarefaction wave. If S_0 goes over the boundary of the transition regime and the MSD regime, M_a will begin to increase, but M_b remains maintaining one. Also in the MSD regime, the head of the thrust pressure region is in contact with the slope of pressure and temperature distribution, and it was confirmed that this slope is a rarefaction wave like the transition regime. Since it is simultaneously set to $M_a>1=M_b$, it is also confirmed that an expansion wave and a heating region separate. Moreover, in the transition regime, since it is $M_a=1$, it also turns out that the heat blockade is caused in the heating region. Moreover, in the transition regime, since $M_a=1$, it also turns out that thermal choking is occurred in the heating region.

3.6 Conclusion

As described above, it was confirmed that distribution of the flow field yielded in Microwave Rocket is constituted from one-dimensional numerical analysis by the shock wave, Rayleigh flow and the rarefaction wave. The structure of the flow field in each regime is constituted from a propagation direction side by the following phenomena at order.

MSC regime

- Shock wave
- Rayleigh flow

Transition regime

- Shock wave
- Rayleigh flow (thermal choking)
- Rarefaction wave

MSD regime

- Rayleigh flow
- Rarefaction wave

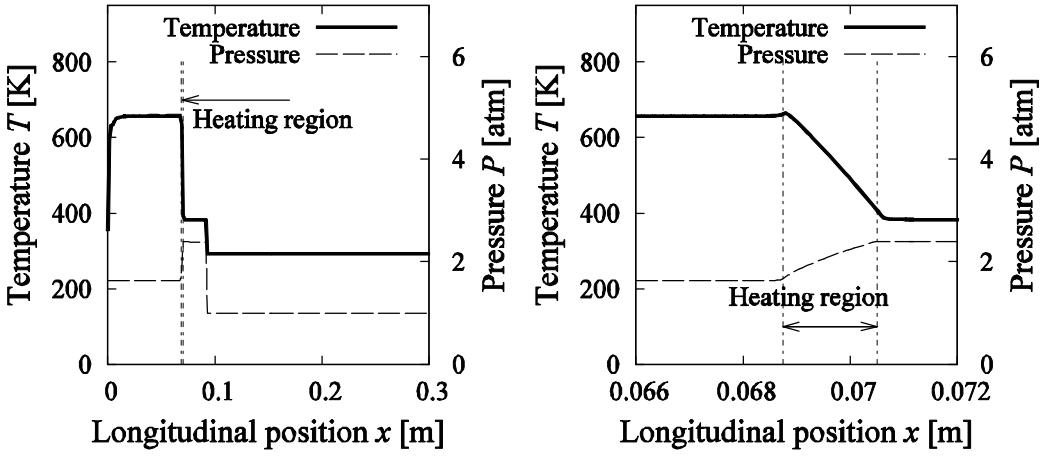

(a) t=0.180[msec]

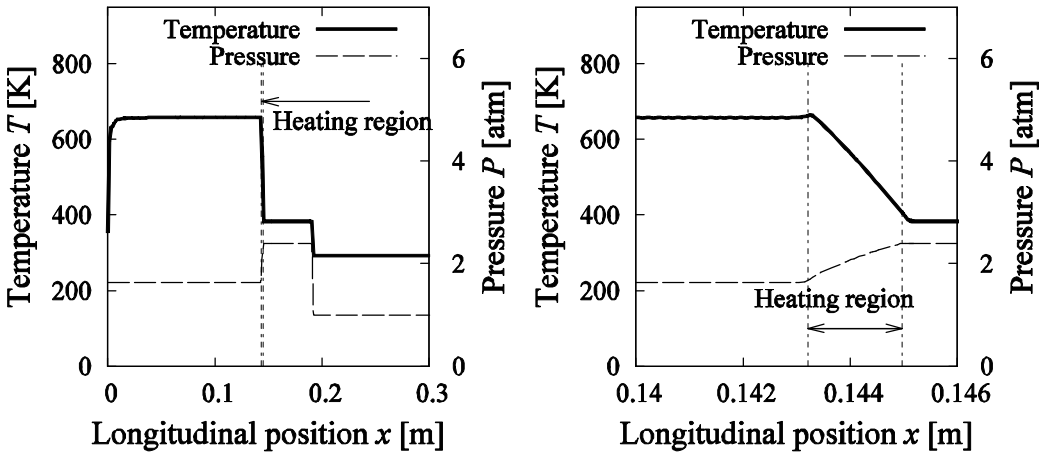

(b) t=0.375[msec]

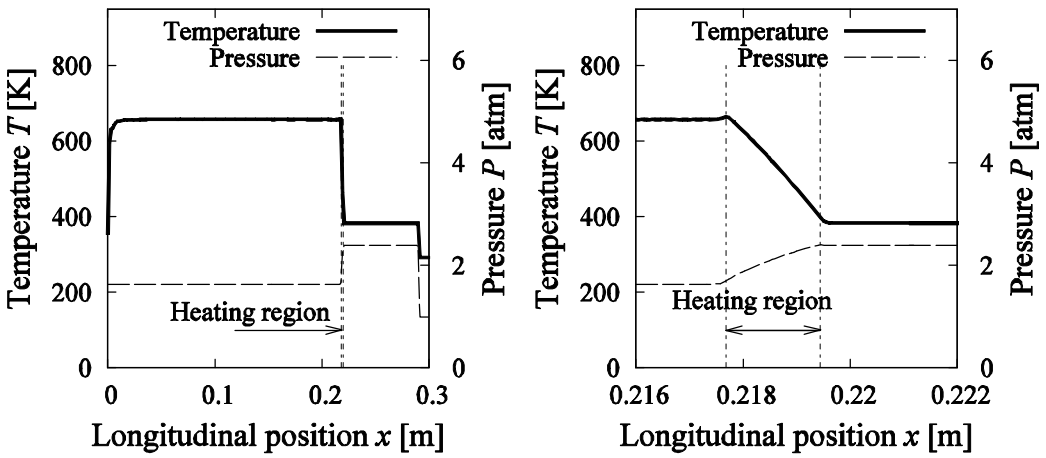

(c) t=0.570[msec]

FIGURE 3.1. Longitudital temperature and pressure distribution in the MSC regime, S_0=100[kW/cm^2]

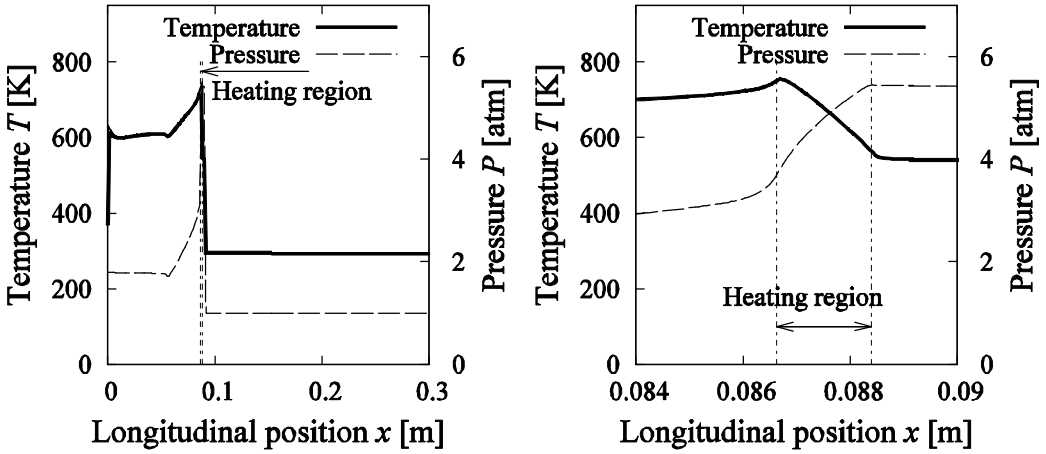

(a) t=0.120[msec]

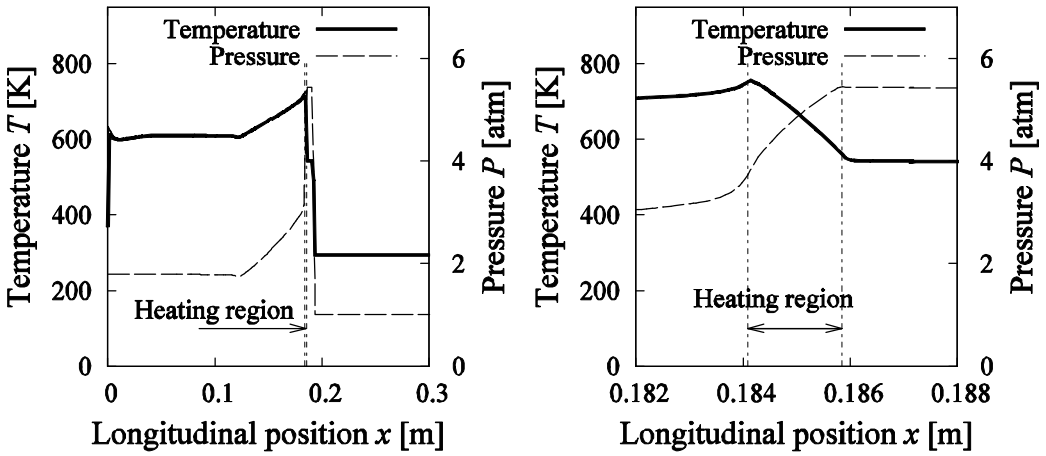

(b) t=0.255[msec]

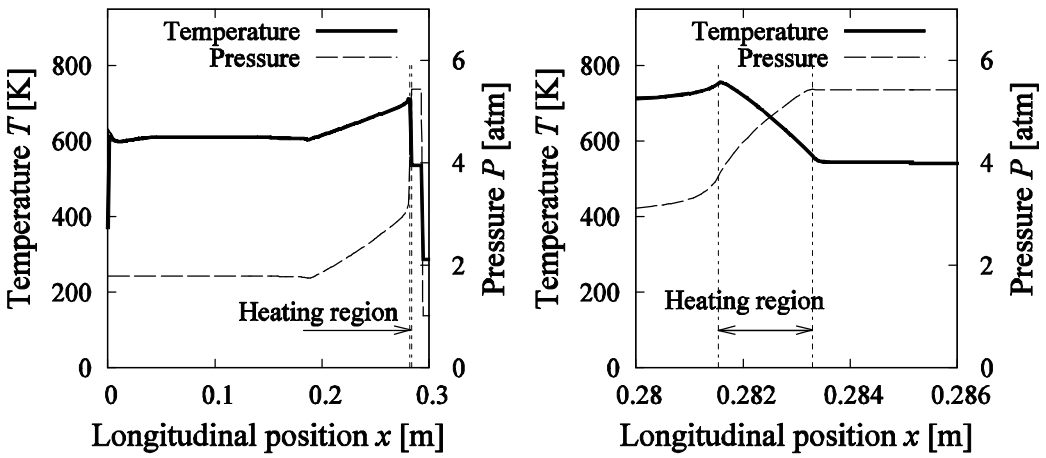

(c) t=0.390[msec]

FIGURE 3.2. Longitudital temperature and pressure distribution in the transition regime, S_0=200[kW/cm^2]

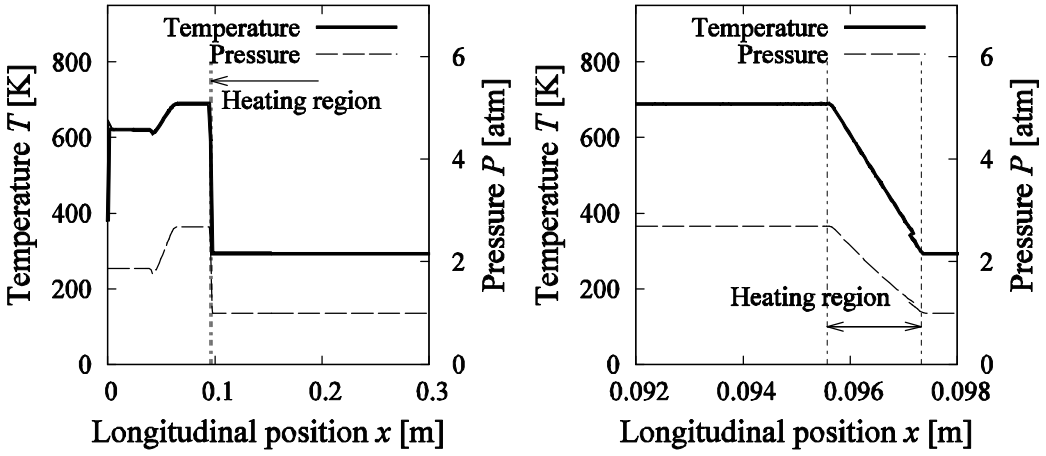

(a) t=0.090[msec]

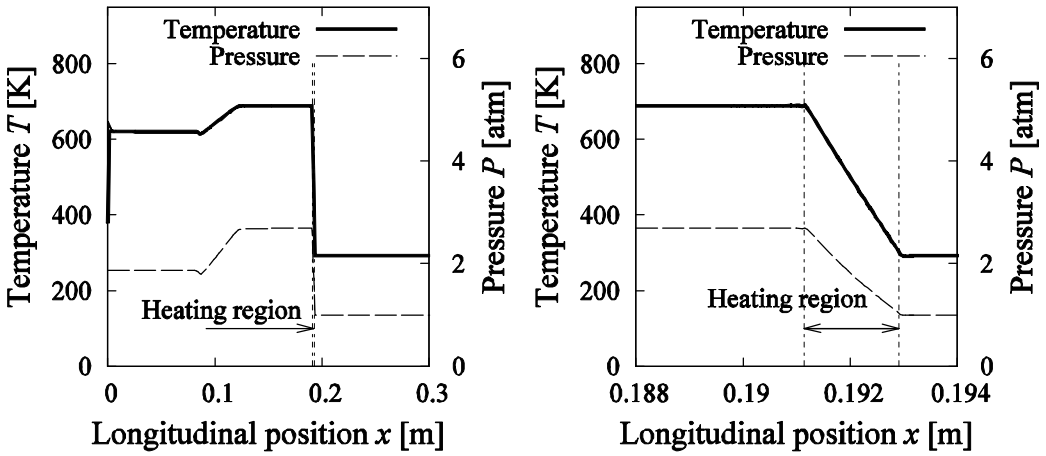

(b) t=0.180[msec]

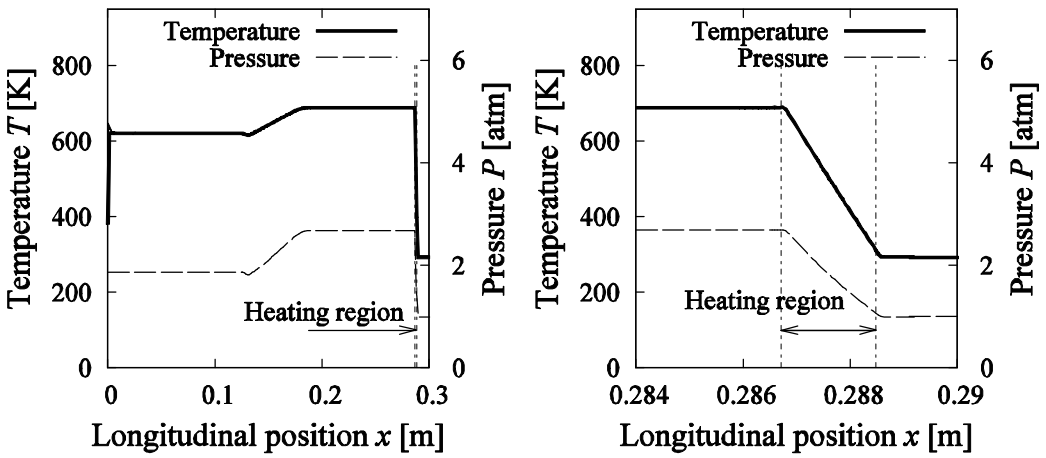

(c) t=0.270[msec]

FIGURE 3.3. Longitudital temperature and pressure distribution in the MSD regime, S_0=300[kW/cm^2]

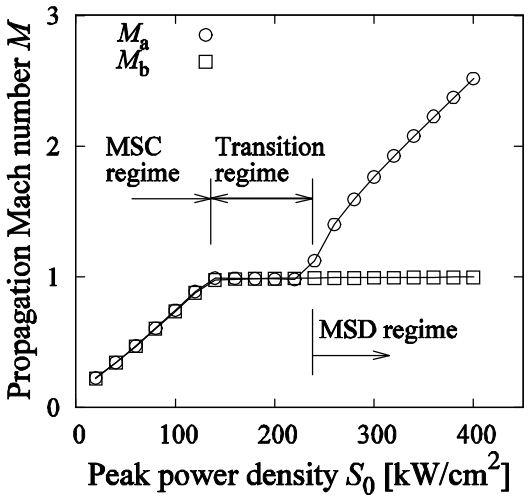

FIGURE 3.4. The propagation Mach number to the local flow velocity of a tail of the ionization front M_a and a head of thrust pressure region M_b

Chapter 4

Theoretical analysis of a microwave supported detonation wave

From the analysis as a result of the one-dimensional numerical computation performed for the foregoing paragraph, it became clear that a microwave support detonation wave is constituted by a shock wave, Rayleigh flow, and the rarefaction wave. Because the analytical solutions about the relations between an inlet flow and an outlet flow of these phenomena are well known [21,22], the flow field inside the Microwave Rocket in which the microwave supported detonation wave propagates can be solved combining these relations. First, the theoretical solution of the flow before and behind three phenomena which compose the microwave supported detonation wave will be shown.

4.1 Shock wave relations

The control volume surrounding a shock wave as shown in FIGURE 4.1 is taken. The shock wave is thin enough and can disregard friction and heating. Therefore, the following primary equations are obtained from the conservation law before and behind the control volume.

$$\rho_{S1} u_{S1} = \rho_{S2} u_{S2} \tag{4.1}$$

$$p_{S1} + \rho_{S1} {u_{S1}}^2 = p_{S2} + \rho_{S2} {u_{S2}}^2 \tag{4.2}$$

$$\frac{\gamma}{\gamma - 1}\frac{p_{S1}}{\rho_{S1}} + \frac{1}{2}{u_{S1}}^2 = \frac{\gamma}{\gamma - 1}\frac{p_{S2}}{\rho_{S2}} + \frac{1}{2}{u_{S2}}^2 = \frac{\gamma + 1}{2(\gamma - 1)}a^{*2} \tag{4.3}$$

The quantities of the inlet flow into the control volume are expressed with a subscript S1, and the quantities of the outlet flow are expressed with a subscript S2. In addition, a^* is the sonic speed in the critical state. Allied the above primary equation and equation of state, the ratio of the temperature, pressure, density, and local flow velocity before and behind a control volume can be obtained as follows.

$$\frac{T_{S2}}{T_{S1}} = \frac{\left\{2\gamma {M_{S1}}^2 - (\gamma - 1)\right\}\left\{(\gamma - 1){M_{S1}}^2 + 2\right\}}{(\gamma + 1)^2 {M_{S1}}^2} \tag{4.4}$$

$$\frac{p_{S2}}{p_{S1}} = \frac{2\gamma {M_{S1}}^2 - (\gamma - 1)}{\gamma + 1} \tag{4.5}$$

$$\frac{\rho_{S2}}{\rho_{S1}} = \frac{u_{S1}}{u_{S2}} = \frac{(\gamma + 1)^2 {M_{S1}}^2}{(\gamma - 1){M_{S1}}^2 + 2} \tag{4.6}$$

M_{S1} is a Mach number of the inlet flow. The expression of relations of the condition before and behind a shock wave is dependent on M_{S1} and a ratio of specific heat γ. Since γ is a constant, if the propagating speed of a shock wave is given, the condition behind the shock wave can be calculated from the condition in front of the shock wave.

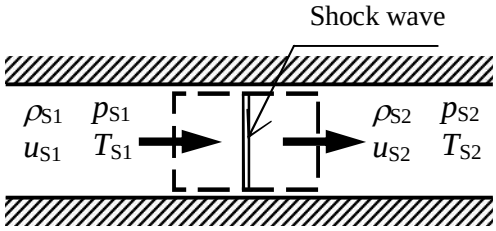

FIGURE 4.1. The control volume surrounding the shock wave

4.2 Rayleigh flow relations

When the heat per unit mass q [J/kg] is added to a control volume as shown in FIGURE 4.2, the conservation law before and behind the control volume is expressed as follows.

$$\rho_{R1}u_{R1} = \rho_{R2}u_{R2} \tag{4.7}$$

$$p_{R1} + \rho_{R1}{u_{R1}}^2 = p_{R2} + \rho_{R2}{u_{R2}}^2 \tag{4.8}$$

$$c_p T_{R1} + \frac{{u_{R1}}^2}{2} + q = c_p T_{R2} + \frac{{u_{R2}}^2}{2} \tag{4.9}$$

The quantities of an inlet flow into the control volume are expressed with a subscript R1, and the quantities of an outlet flow is expressed with a subscript R2. Heat per unit mass added into flow by microwave q [J/kg] can be evaluated as follows.

$$q = \frac{\eta S_{average}}{\rho_{R1}u_{R1}} \tag{4.10}$$

Using the above primary equations, the density, flow velocity, and the pressure ratio before and behind the control volume are solved as follows:

$$\frac{\rho_{R1}}{\rho_{R2}} = \frac{u_{R2}}{u_{R1}} = \frac{1+\gamma{M_{R1}}^2}{(\gamma+1){M_{R1}}^2} + \left\{\frac{{M_{R1}}^2-1}{(\gamma+1){M_{R1}}^2}\right\}\sqrt{1-\frac{Q}{Q_{max}}} \tag{4.11}$$

$$\frac{p_{R2}}{p_{R1}} = \frac{1+\gamma{M_{R1}}^2}{\gamma+1} - \left\{\frac{\gamma\left({M_{R1}}^2-1\right)}{\gamma+1}\right\}\sqrt{1-\frac{Q}{Q_{max}}} \tag{4.12}$$

$$Q = \frac{q}{c_p T_{R01}} \tag{4.13}$$

$$Q_{max} \equiv \frac{\left({M_{R1}}^2-1\right)^2}{(\gamma+1){M_{R1}}^2\left\{2+(\gamma+1){M_{R1}}^2\right\}} = \frac{q_{max}}{c_p T_{R01}} \tag{4.14}$$

M_{R1} is a Mach number of an inlet flow to the control volume shown in FIGURE 4.2. T_{0R1}[K] is the total temperature of an inlet flow. q_{max}[J/kg] expresses the amount of heating per unit mass in case the outflow Mach number is set to 1 and a thermal choke occurs. Q, Q_{max} are normalized q, q_{max} by specific enthalpy of the inlet flow $c_p T_{0R1}$, respectively. Using the measured amount of heating by the microwave and propagating speed of the heating region, if the density, flow velocity, pressure, and temperature of the inlet flow are already-known, the condition of the outlet flow can be calculated with the above relations.

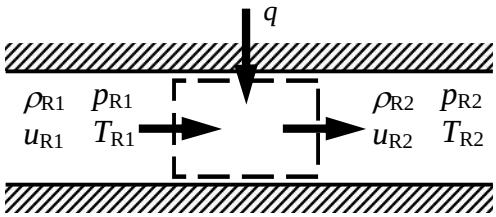

FIGURE 4.2. The control volume surrounding the heating region

4.3 Rarefaction wave relations

The one-dimensional forward running rarefaction wave propagates in the positive direction of x is shown in FIGURE 4.3. The quantities of the flow in front of the rarefaction wave are expressed with a subscript E1, the quantities of the flow behind the wave are expressed with a subscript E2, and the gas behind the wave assumes at rest.

Because the Riemann invariant and entropy are constant in the rarefaction wave, the following primary equations are obtained.

$$u-\frac{2a}{\gamma-1}=u_1-\frac{2a_1}{\gamma-1}=-\frac{2a_2}{\gamma-1} \tag{4.15}$$

$$\frac{a}{a_1}=\left(\frac{T}{T_1}\right)^{\frac{1}{2}}=\left(\frac{p}{p_1}\right)^{\frac{\gamma-1}{2\gamma}}=\left(\frac{\rho}{\rho_1}\right)^{\frac{\gamma-1}{2}} \tag{4.16}$$

Therefore, the density, pressure and temperature ratio before and behind the rarefaction wave are

$$\frac{T_{E2}}{T_{E1}}=\left(1-\frac{\gamma-1}{2}M_{E1}\right)^2 \tag{4.17}$$

$$\frac{p_{E2}}{p_{E1}}=\left(1-\frac{\gamma-1}{2}M_{E1}\right)^{\frac{2\gamma}{\gamma-1}} \tag{4.18}$$

$$\frac{\rho_{E2}}{\rho_{E1}}=\left(1-\frac{\gamma-1}{2}M_{E1}\right)^{\frac{2}{\gamma-1}} \tag{4.19}$$

M_{E1} is a Mach number of the flow velocity in front of the rarefaction wave shown in FIGURE 4.3. Using these relations which depend on M_{E1} and a ratio of specific heat γ, the condition behind the rarefaction wave can be calculated from the condition in front of it.

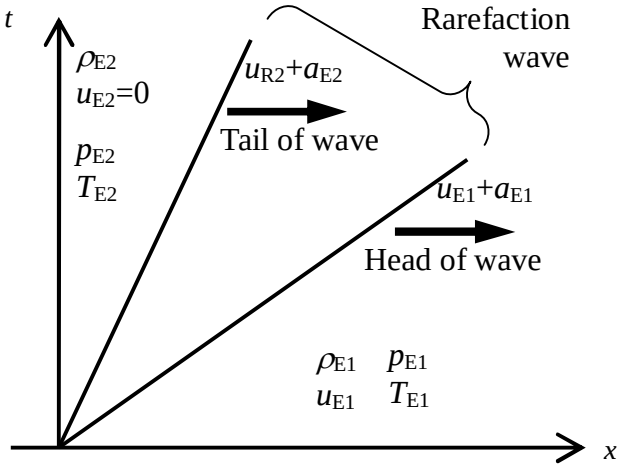

Figure 4.3. Forward running rarefaction wave

The flow field in the Microwave Rocket in each regime is solved with combining the relations between above three phenomena.

4.4 MSC regime

The shock wave precedes the heating region in the MSC regime. The flow field can be expressed by the equations (4.4-6) and the equations (4.11-14). Not to given the shock wave propagating speed U_{shock} we cannot obtain the flow field directly. However, the thrust pressure region behind the heating region contacts with the thrust wall. It can be set to u_3=0. Therefore, the flow field can be obtained by using variable U_{shock}, and calculating iterative calculation until the solution as u_3=0 is obtained.

4.5 Transition regime

In this regime, the shock wave, the heating region, and the rarefaction wave propagate sequentially and there is the thrust pressure region bihind the rarefaction wave. The equations (4.4-6), (4.11-14) and (4.17-19) can express the flow field.

Although the shock wave propagating speed U_{shock} is not given like the MSC regime, it is confirmed that a thermal choke occurs in a heating region in this regime. The flow field can be obtained by giving variable U_{shock} and performing iterative calculation until the solution as Q_{max}=Q in the equations (4.13, 14) is obtained. Such operation is used for an equation (4.17-19), and the condition in front of the rarefaction wave is acquired. Furthermore, the condition of the thrust pressure region is acquired from an equation (4.17-19). In this way, whole the flow field in this regime can be calculated.

4.6 MSD regime

The flow field of MSD regime which a heating region precedes in front of the rarefaction wave is expressed by the equations (4.11-14) and (4.17-19). The propagating

speed of a heating region obtained by the empirical equation (2.61) is given. Not using iterative operation, whole the flow field in this regime can be solved directly from the gas at rest.

4.7 Determination of the boundary between each regime

In the MSC regime, the flow velocity of the direction of the open end generated by the shock wave is accelerated for reverse in the heating region. And the velocity becames rest. S_0 exceeding some value, a thermal choke will occur in the heating region and solution as u_3=0 can't be obtained with itarative oparation. Then, the region which satisfies $Q>Q_{max}$ in the heating region which shock wave behind satisfies can be determined as the MSC regime.

In the MSD regime the heating region precedes and propagates at supersonic speed. S_0 going down some value, a thermal choke will occur in the heating region. Because a precedence heating region can not absorb adding heat q with a thermal choke, a shock wave precedes and the inflow conditions to the heating region change. This is a change to the transition regime. Then the region which satisfies $Q>Q_{max}$ in the heating region to precede can be determined as the MSD regime.

Furthermore, in the transition regime, the Mach number just behind the heating region is M_a=1 and the thermal choke has always occurred. It is set to $Q=Q_{max}$. Distribution of Q and Q_{max} every S_0 is shown in FIGURE 4.4.

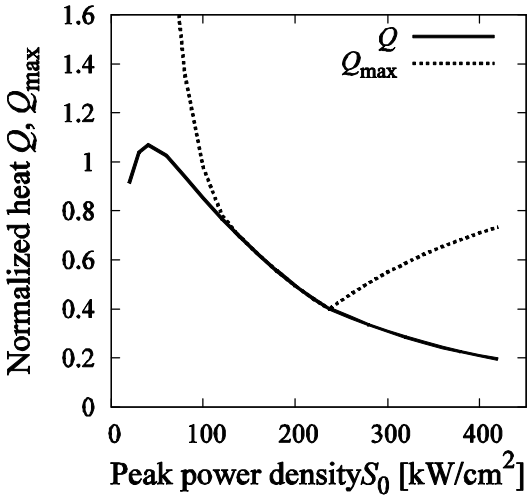

FIGURE 4.4. Distribution of Q, Q_{max}

From the graph, the range of each regime is determined as follows:

- MSC regime S_0<136[kW/cm^2]
- Transition regime 136≦S_0≦238[kW/cm^2]
- MSD regime S_0>238[kW/cm^2]

With the application of the equations (4.4-6), (4.11-14), and (4.17-19) for every ranges of these regimes, the theoretical solution of the flow field can be calculated. Comparison with the result of the numerical analysis about the pressure p_3 in the thrust pressure region and the sonic speed a_3 is shown in FIGURE 4.5 and 4.6, respectively. a_3 is equal to the speed of the rarefaction wave which enters into the thruster from the open

end side.

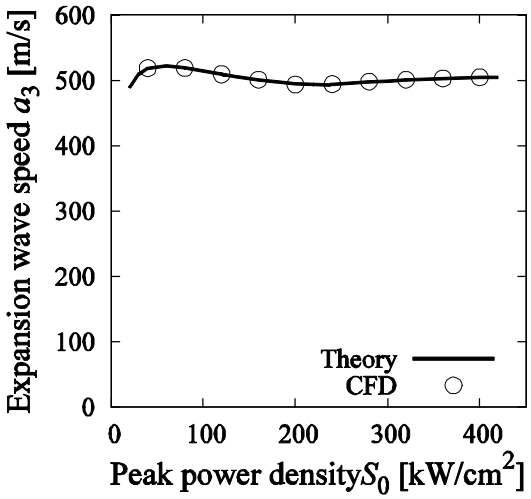

FIGURE 4.5. Validation of theoretical results using p_3

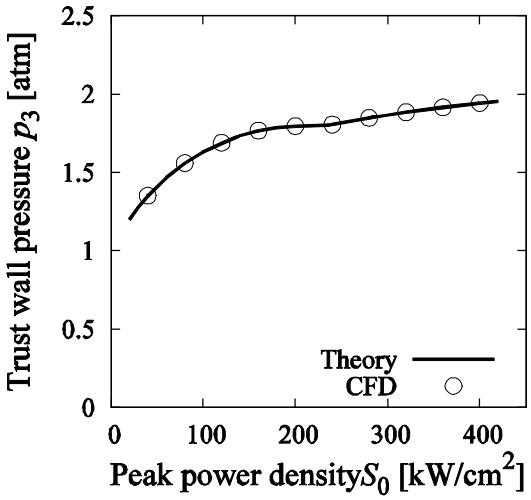

FIGURE 4.6. Validation of theoretical results using a_3

As for pressure p_3 and the sonic speed a_3, the theoretical solution shows good coincidence as the numerical analysis result, and the confirmation of the theory was obtained in all the regimes

Thereby, I solved the structure of the microwave supported detonation wave.

Chapter 5

Comparison with a chemical detonation

5.1 A structure of the chemical detonation wave

Chemical detonation is a phenomenon in which a shock wave following a combustion region propagates thruough a combustible mixture at high speed. The structural model of chemical detonation is known as a ZND detonation model. This model is researched by Zel'dovich (1940), von Neumann (1942) and Doring (1943) independently and is called ZND model. In the case of stable detonation propagating at a fixed speed, the propagationg shock wave heats unburned gas to high temperature, and induces combustion.

Therefore, as shown in FIGURE 5.1 it can be considered that the detonation wave is composed of a region a-b in which density, pressure, and temperature are increased rapidly by the shock wave without a reaction and a heating region c-d following shock wave at same speed. And there is the slight time delay between two regions. Seeing from the coordinate system which fixed the shock wave a-b, in the heating region cd, since its back is subsonic pressure and density will decrease and temperature will increase like a subsonic Rayleigh flow.

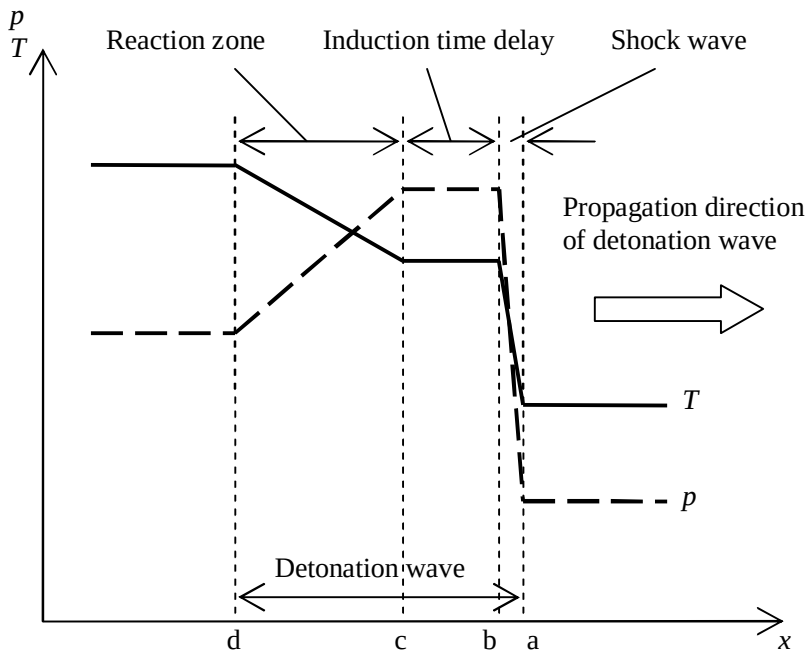

FIGURE. 5.1 Structure of the chemical detonation wave

The shock wave a-b and the combustion region c-d propagating at uniform speed, the chemical detonation can be considered the heating flow that reaction heat supplied in the control volume surrounding whole the detonation wave a-d. Therefore,

in the flow field before and behind a detonation wave, (4.8-10) of Rayleigh flow relations can be applied.

Using the equations (4.8,9) and specific volume $v=1/\rho$

$$p_{R2} - p_{R1} = -\frac{\gamma p_{R1}}{v_{R1}} M_{R1}\left(v_{R2} - v_{R1}\right) \qquad (5.1)$$

Generalizing with $p=p_{R2}$, $v=v_{R2}$

$$\frac{p}{p_{R1}} = \left(1+\gamma M_{R1}{}^2\right) - \gamma M_{R1}{}^2 \frac{v}{v_{R1}} \qquad (5.2)$$

The line which this equation draws on a *p*-*v* diagram is called Rayleigh line.

Moreover, from the equations (4.8-10)

$$\frac{\gamma+1}{\gamma-1}\left(p_{R2}v_{R2} - p_{R1}v_{R1}\right) = p_{R2}v_{R2} - p_{R1}v_{R1} + q \qquad (5.3)$$

Generalizing with $p=p_{R2}$, $v=v_{R2}$ like Rayleigh line

$$\frac{p}{p_{R1}} = \left(\frac{\gamma+1}{\gamma-1} - \frac{v}{v_{R1}} + \frac{2q}{p_{R1}v_{R1}}\right) \Bigg/ \left(\frac{\gamma+1}{\gamma-1}\frac{v}{v_{R1}} - 1\right) \qquad (5.4)$$

The curve which this equation draws on a *p*-*v* diagram is called Hugniot curve. Assuming $q= 0$ the equations (4.8-10) correspond to the primary equation before and behind a shock wave. Therefore, the Hugniot curve with $q= 0$ is called a shock adiabatic. The Rayleigh line, the Hugniot curve, and the shock adiabatic on a *p*-*v* diagram are shown in FIGURE 5.2.

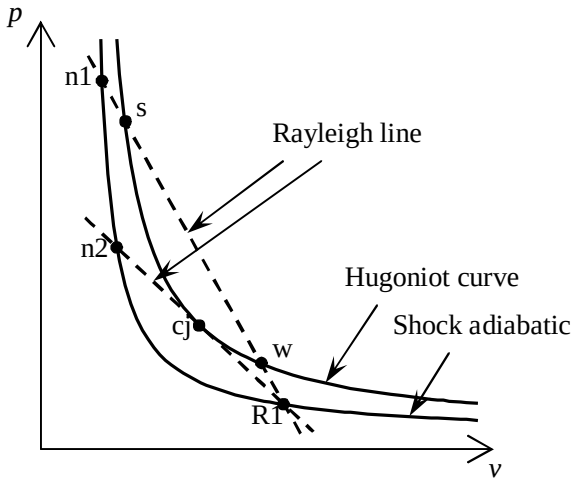

FIGURE 5.2. *p*-*v* diagram

A precedence shock wave changes along a shock adiabatic the condition of a flow field from the initial condition in front of the detonation wave which corresopnd a point R1 to the intersection n1 or n2 of a shock adiabatic with a Rayleigh line. Then, condition changes to the intersection s or cj with a Hugoniot curve along with a Rayleigh line in the heating region by combustion. Although the Rayleigh line containing n1 and s has an intersection with a Hugoniot curve also at point w, a rarefaction shock wave corresponding to change from s to w can not exist. Then the chemical detonation which changes to w can not exist.

Because of the equation (5.2) gradients of Rayleigh lines are determined by inflow Mach-number M_{R1}. The point cj corresponding to the downstream of a chemical detonation which has the smallest M_{R1} in other words which has the slowest speed propagating into a rest gas is called a C-J (Chapman-Jouget) state, and such a detonation is called a C-J detonation. The measurement result of the propagating speed of a self propagating detonation is well agreed with the speed of the C-J detonation. A detonation which is expressed with point s is generated when attenuation of a wave is covered with a piston etc. from wave face behind.[21,22]

5.2 Behavior of states on the p-v diagram in every regime of the microwave supported detonation

The *p*-*v* diagram at S_0=100[kW/cm^2] showing the pressure and temperature distribution of the thruster longitudinal direction in FIGURE 3.1 is shown in FIGURE 5.3. Points 1, 2, 3 on FIGURE 7 shows the initial state 1, the state 2 maintained between the shock wave and the heating region, and the state 3 in the thrust pressure region behind heating region, respectively.

S_0=100[kW/cm^2] is in the MSC regime, the shock wave and heating region propagating separately, it is necessary to take two control volumes into consideration. The change from the point 1 to the point 2 on FIGURE 5.3 corresponds to the shock wave, and a state changes to the intersection with the Rayleigh line 1 along the shock adiabatic. Heating causes the change to the point 3 from the point 2, and a state changes to the intersection with a Hugoniot line along the Rayleigh line 2. In this case, inlet conditions differ in the shock wave and the heating region. A shock adiabatic and a Rayleigh line 1 make inlet conditions the state 1 and the propagating speed of the shock wave, and a Rayleigh line 2 and a Hugoniot curve make inlet conditions the state 2 and the propagating speed of the heating region.

As an example of the transition regime, the *p*-*v* diagram in S_0=200[kW/cm^2] showing the pressure and temperature distribution of the thruster longitudinal direction in FIGURE 3.2 is shown in FIGURE 5.4. Points 1, 2, 2.5, 3 on FIGURE 5.4 shows the initial state 1, the state 2 maintained between the shock wave and the heating region, the state 2.5 just behind the heating region, and the state 3 in the thrust pressure region behind the rarefaction wave, respectively.

In the transition regime, the shock wave and the heating region propagating separately like the MSC regime, a shock adiabatic line and a Rayleigh line 1 which make inlet conditions the state 1 and the propagating speed of the shock wave, and a Rayleigh line 2 and a Hugoniot curve which make inlet conditions the state 2 and the propagating speed of the heating region. The shock wave causes the change to the point 2 from a point 1 on FIGURE 5.4, and a state changes to the intersection with the Rayleigh line 1 along the shock adiabatic. Heating causes the change to the point 2.5 from the point 2, and a state changes to the contact with the Hugoniot curve along the Rayleigh line 2.

Adding heat per unit mass q of the equation (5.4) becoming larger, the Hugoniot curve will move to the upper right on the *p*-*v* diagram. That is, the contact with a convex downward Hugoniot curve means the point of obtaining the maximum heat per unit mass q on the Rayleigh line. In the transition regime, the maximum heat

that can be added to the inlet flow in the heating region is added, and a thermal choke occurs. For this reason, the Rayleigh line 2 and a Hugoniot curve touch by one point.

Next, the *p*-*v* diagram in S_0=300[kW/cm^2] showing the pressure and temperature distribution of thruster longitudinal direction in FIGURE 3.3 is shown in FIGURE 5.5. Points 1, 2, 3 on FIGURE 5.5 show the initial state 1, the state 2 maintained between the heating region and the rarefaction wave, and the state 3 in thrust pressure region behind the rarefaction wave, respectively.

S_0=100[kW/cm^2] is in the MSD regime, a shock wave is not generated but only the heating region propagates. The heating caouses the change to the point 2 from the point 1 on FIGURE 5.5, and a state changes to the intersection with a Hugoniot line along a Rayleigh line. The point 2 is unanimous with the point w shown in FIGURE 5.2. This state is in the state which is not realized because change by the rarefaction shock wave from the point s does not exist in the case of the chemical detonation which the shock wave must precede with the heating region. It can be called the phenomenon peculiar to the MSD regime in which only the heating region propagates.

5.3 The chemical detonation wave and the microwave supported detonation wave

In the microwave supported detonation wave, the shock wave precedes the region heated by microwave in MSC regime and Transition regime, as well as a chemical detonation. In particular, near the boundary with the MSD regime in the transition regime, the propagating speed of a shock wave and an ionization front is mostly unanimous. The structure similar to the ZND detonation model which the shock wave to precede and the heating region to follow it approach is found.

A pressure and temperature distribution of the thruster longitudinal direction of S_0=225[kW/cm^2] near the boundary with the MSD regime in the transition regime are shown in FIGURE 5.6, and a *p*-*v* diagram is shown in FIGURE 5.7 , respectively. Points 1, 2, 2.5, 3 on FIGURE 5.7 show the initial state 1, the state 2 maintained between the shock wave and the heating region, the state 2.5 just behind the heating region, and the state 3 in the thrust pressure region behind the rarefaction wave, respectively.

The distribution at the time t=0.315[msec] shown in FIGURE 5.6 (c) bears it of the ZND detonation model. Because the shock wave and the heating region separate gradually, a Rayleigh line and a Hugoniot curve do not have a contact on the *p*-*v* diagram, but the state 2.5 is on the point that two lines approach. It was found that the phenomenon similar to the C-J detonation occurs. On the other hand, the flow field which is unanimous with C-J conditions is obtained in the boundary of the transition regime and the MSD regime which were calculated from the range in which a thermal choke occurs. Its boundary is S_0=238[kW/cm^2]. The pressure and the temperature distribution of the thruster longitudinal direction in this case are shown in FIGURE 5.8, and a *p*-*v* diagram is shown in FIGURE 5.9, respectively. Points 1, 2, 3 of FIGURE 5.9 show the initial state 1, the state 2 just behind the heating region, and the state 3 in the thrust pressure region behind the rarefaction wave, respectively.

A preceding shock wave is not generated but only the heating region propagates as shown in FIGURE 5.8. Unlike the ZND detonation model, a state changes from the state 1 to the C-J point directoly along the Rayleigh line on the *p*-*v* diagram of

FIGURE 5.9. The C-J condition is satisfied without being accompanied by the rapid pressure rise due to a shock wave.

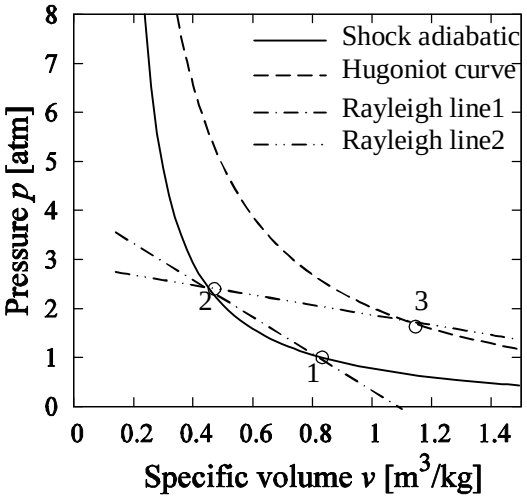

FIGURE 5.3. Every states on *p*-*v* diagram in the MSC regime, S_0=100[kW/cm^2]

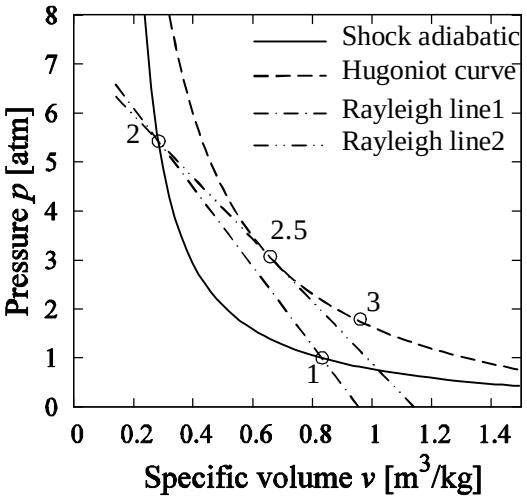

FIGURE 5.4. Every states on *p*-*v* diagram in the transition regime, S_0=200[kW/cm^2]

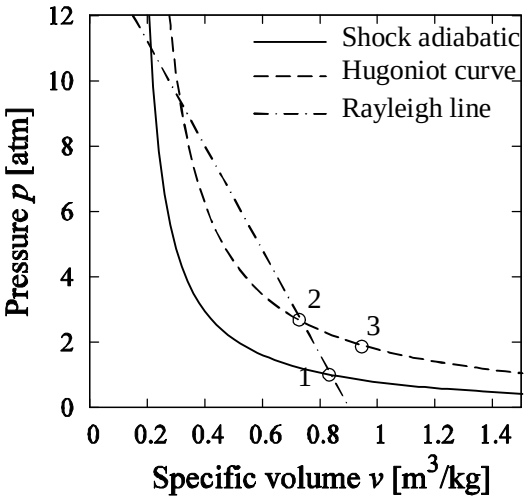

FIGURE 5.5. Every states on *p*-*v* diagram in the MSD regime, S_0=300[kW/cm^2]

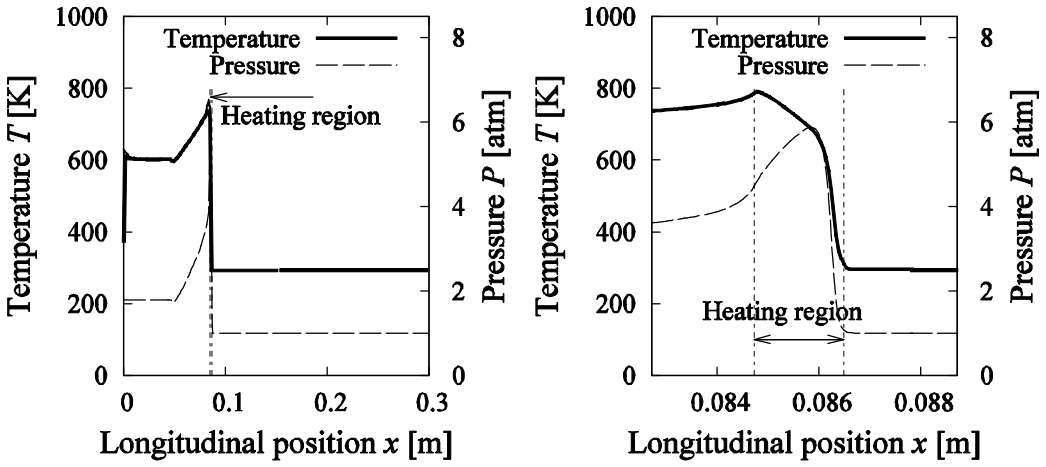

(a) t=0.105[msec]

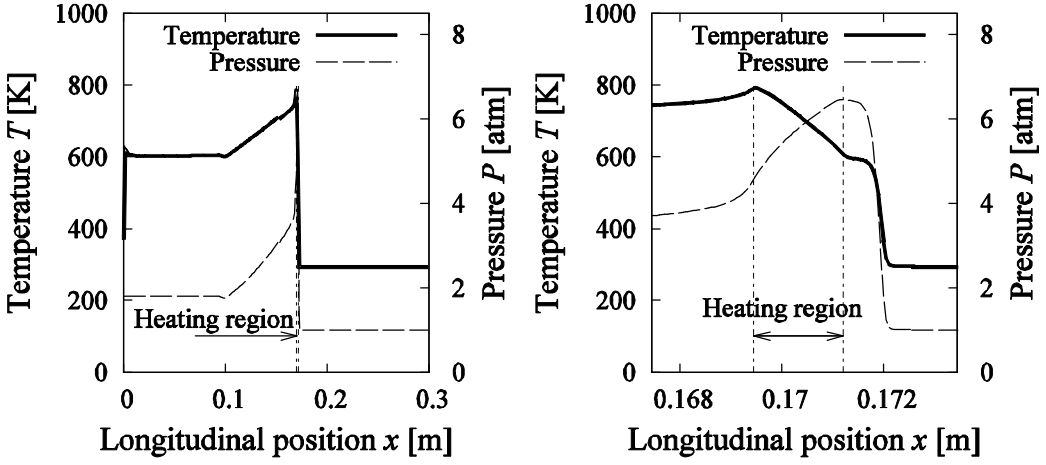

(b) t=0.210[msec]

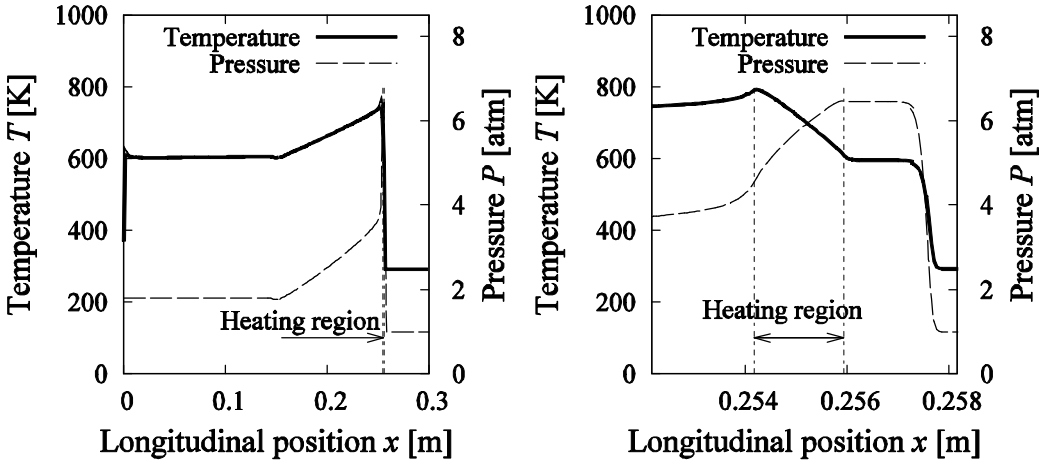

(c) t=0.315[msec]

FIGURE 5.6. Longitudital temperature and pressure distribution in the MSC regime, S_0=225[kW/cm^2]

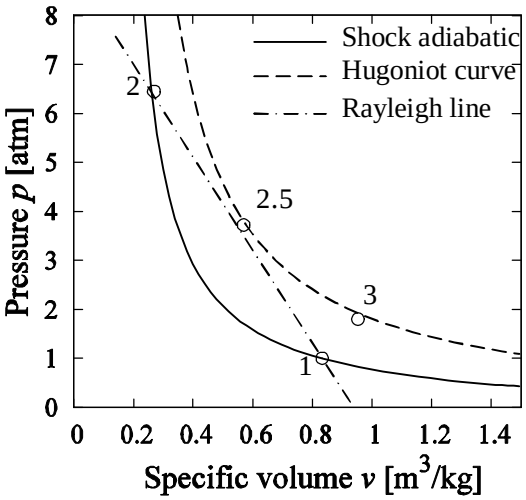

FIGURE 5.7. Every states on *p*-*v* diagram in the MSC regime, S_0=100[kW/cm^2]

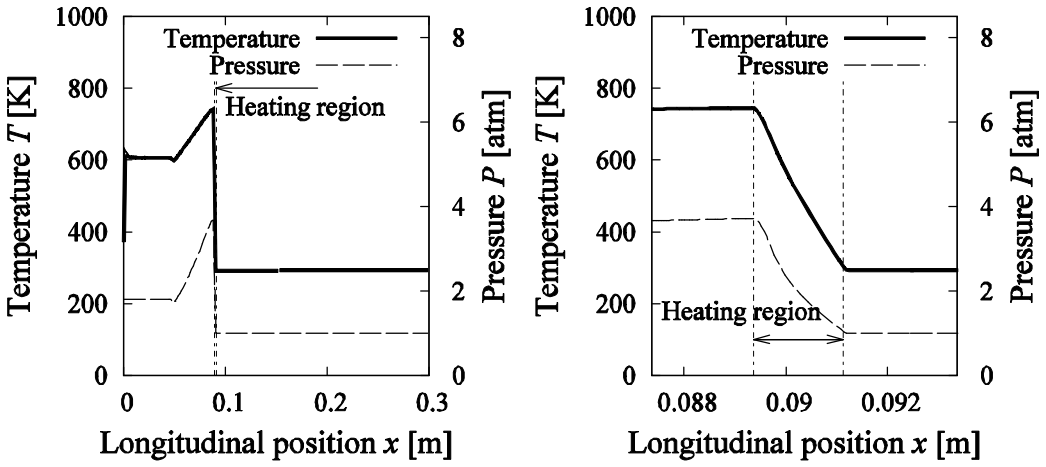

(a) t=0.105[msec]

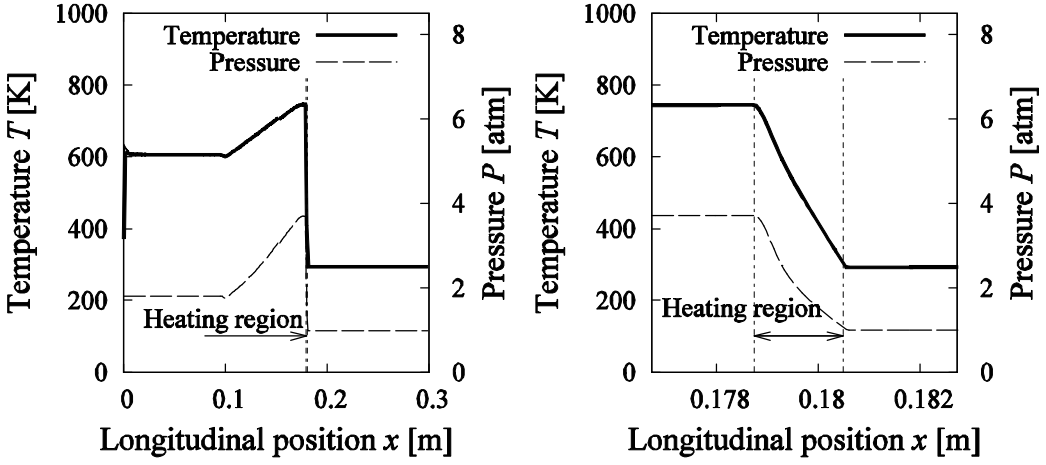

(b) t=0.210[msec]

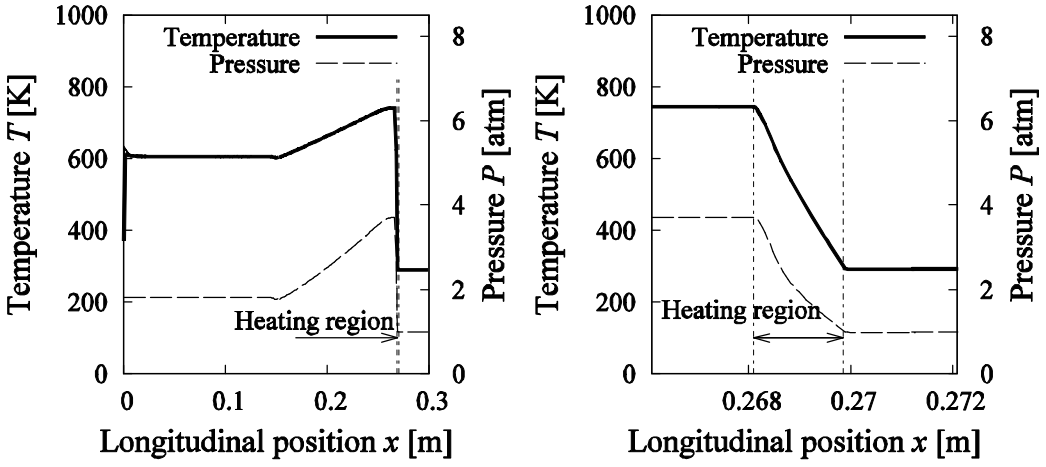

(c) t=0.315[msec]

FIGURE 5.8. Longitudital temperature and pressure distribution in the transition regime, S_0=238[kW/cm^2]

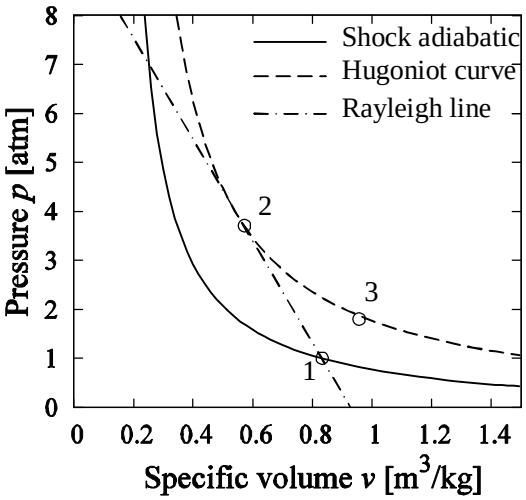

FIGURE 5.9. Every states on *p*-*v* diagram in the MSC regime, S_0=100[kW/cm^2]

Chapter 6

Conclusion

In this research Using measured the ionization front velocity U_{ioniz} CFD simulation was performed. This simulation method doesn't need to assume any specific heat constant for microwave heating process.

Results of one-dimensional numerical analysis are well agreed with those of experiments.

Using the very simplified method with measured U_{ioniz} one-dimensional numerical simulation of the flow field in Microwave Rocket which the microwave supported detonation wave propagates was conducted. The results of numerical analysis and experiments were compared about the pressure p_3 and the sound speed a_3 in the trust pressure region, and the validity of the numerical analysis results was verified.

The magnitude and tendency of the numerical analysis result of p_3 and a_3 are well agreed with the experimental result well. The simplified method enabled observation of the changes of the state by the microwave supported detonation wave.

The flow field which the microwave supported detonation wave propagates consists of three phenomena.

Distribution along the thruster longitudinal direction of the states in the thruster generated by heating to the ionization front by microwave can be categorized into three regimes according to the power density of microwave S_0. These regimes are a microwave supported combustion (MSC) regime, a transition regime and a microwave supported detonation (MSD) regime.

Analyzing the results of one-dimensional simulation, it is confirmed that the structure of the flow field in each regime is constituted from a propagation direction side by the following phenomena at order.

MSC regime

- Shock wave
- Rayleigh flow

Transition regime

- Shock wave
- Rayleigh flow (thermal choking)
- Rarefaction wave

MSD regime

- Rayleigh flow
- Rarefaction wave

The structure of the microwave supported detonation wave was given theoretical solution.

Well known theoretical solutions about the relations between an inlet flow and an outlet flow of these phenomena, a shock wave, Rayleigh flow, and a rarefaction wave were combined. the flow field inside the Microwave Rocket in which the microwave supported detonation wave propagates were the given theoretical solution. And from the thermal choking condition, the boundaries between each regimes are figured out as follows.

- MSC regime $S_0<136[kW/cm^2]$
- Transition regime $136 \leqq S_0 \leqq 238[kW/cm^2]$
- MSD regime $S_0>238[kW/cm^2]$

The microwave supported detonation wave which satisfies C-J condition was found.

Near the boundary with the MSD regime in the transition regime, the propagating speed of a shock wave and an ionization front is mostly unanimous. The structure is similar to the ZND detonation model which the shock wave to precede and the heating region to follow it approach. And on the boundary of the transition regime and the MSD regime, $S_0=238[kW/cm^2]$, the microwave supported detonation wave satisfies C-J condition.

References

1. Brikan M.A., "Laser Propulsion: Research Status and Needs", Journal of Propulsion and Power, 8, (1992), pp. 354-360
2. Kantrowitz A., "Propulsion to Orbit by Gronund-Based Lasers", Astronautics and Aeronautics, pp. 74-76, 1972
3. Raizer Y.P., "Laser-Induced Discharge Phenomena", Consultants Bureau, New York and London, 1977, Ch.6
4. Myrabo L.N., Messitt D.G. and Mead F.G.Jr, "Ground and Flight Test of a Laser Propelled Vehicle", AIAA Paper 98-1001, 1998
5. Myrabo L.N., "World Record Flights of Beam-Riding Rocket Lightcraft - Demonstration of “Disruptive” Propulsion Technology", AIAA Paper 01-3798, 2001
6. K. Sakamoto, A. Kasugai, K. Takahashi, R. Minami, N. Kobayashi, and K. Kajiwara, Nature Pysics, 3(6):411-414, 2007
7. A. Kasugai, K. Sakamoto, R. Minami, K. Takahashi, and T. Imai, "Study of millimeter wave high-power gyrotron for long pulse operation", Nuclear Instrument and Method in Physics Research A, 528:110-114, 2004
8. K. Sakamoto, "Application of plasma heating technology for frontier science", Proceedings of Plasma Science Symposium 2005 and The 22nd symposium on Plasma Proceeding, 2005
9. Nakagawa T., Mihara Y., Komurasaki K., Takahashi K., Sakamoto K., and Imai T., "Propulsive Impulse Measurement of a Microwave-Boosted Vehicle in the Atmosphere", Journal of Spacecraft and Rockets, Vol. 41, 2004, pp. 151-153
10. Katsurayama H., Komurasaki K., and Arakawa Y., "Feasibility for the Orbital Launch by Pulse Laser Propulsion", Journal of Space Technology and Science, Vol. 20, No. 2, 2005, pp. 32-42
11. Oda Y., Ushio M., Komurasaki K., Takahashi K., Kasugai A., and Sakamoto K., "A Multi Pulsed Flight Experiment of a Microwave Beaming Thruster", 3rd International Symposium on Beamed Energy Propulsion, Troy, NY, 2004, pp. 295-302
12. Oda Y., Ushio M., Komurasaki K., Takahashi K., Kasugai A., and Sakamoto K., "Pressure History Measurement in a Microwave Beaming Thruster", 4th International Symposium on Beamed Energy Propulsion, Nara, Japan, 2005
13. Oda Y., Komurasaki K., Takahashi K., Kasugai A., and Sakamoto K., "Experimental study on microwave beaming propulsion using a 1MW-class gyrotron", 56th International Astronautical Congress, Fukuoka, Japan, 2005
14. Oda Y., Kawamura K., Komurasaki K., Takahashi K., Kasugai A., and Sakamoto K., "An Experimental Study on a Thrust Generation Model for Microwave Beamed Energy Propulsion", AIAA 2006-0765
15. Oda Y., Shibata T., Komurasaki K., Takahashi K., Kasugai A., and Sakamoto K., "A Plasma and Shockwave Observation with Pulse Repetition in a Microwave Boosted Thruster", AIAA 2006-4631
16. Oda Y., Shibata T., Komurasaki K., Takahashi K., Kasugai A., and Sakamoto K., "An Experimental Observation for the Shock Wave Driven by Atmospheric Microwave Plasma in a Microwave Rocket", AIAA 2007-4592
17. Oda Y., Shibata T., Komurasaki K., Takahashi K., Kasugai A., and Sakamoto K., "A thrust generation model of microwave rocket", Journal of Space Technology and Science (in print)
18. Bussing T., and Pappas G., "An Introduction to Pulse Detonation Engines", AIAA 94-0263 (1994)
19. Endo T., Kasahara J., Matsuo A., Inaba K., Sato S., and Fujiwara T., "Pressure History at the Thrust Wall of Simplified Pulse Detonation Engine", AIAA Journal, Vol. 42, No. 9, 2004, pp. 1921-1930
20. Graham Candler, "Finite Volume Methods in Computational Fluid Dynamics", transcript of a lecture, Aerospace Engineering and Mechanics, University of Minnesota, 1995
21. **松尾 一泰**, "**圧縮性流体力学 内部流れの理論と解析**", **理工学社**, 1994
22. Landau L.D. and Lifshitz E.M., "Fluid Mechanics, 2nd ed.", Butterworth-Heinemann, Oxford, 1987

修士論文に関する発表一覧

1. **柴田鉄平, 小田靖久, 小紫公也, 高橋幸司, 春日井敦, 坂本慶司, “マイクロ波ロケットの推力発生モデルへの給排気過程の影響”, 平成 19 年度宇宙輸送シンポジウム**, January 18-19, 2007, **相模原**

2. **柴田鉄平, 小田靖久, 小紫公也, 高橋幸司, 春日井敦, 坂本慶司, “パルスデトネーション駆動マイクロ波ロケットのマルチパルス運転”, 平成１８年度衝撃波シンポジウム**, March 15-17, 2007, **福岡**

3. Teppei Shibataa, Yasuhisa Oda, Kimiya Komurasakia and Yoshihiro Arakawa, “A Numerical Simulation of the Energy Conversion Process in Microwave Rocket”, Fifth International Symposium on Beamed Energy Propulsion, November 12 - 15, 2007, Hawaii